



CHALMERS
UNIVERSITY OF TECHNOLOGY

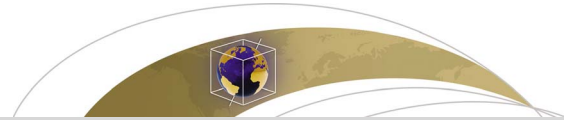
Evolution of the 2015 Cotopaxi Eruption Revealed by Combined Geochemical & Seismic Observations

Downloaded from: <https://research.chalmers.se>, 2026-05-21 17:34 UTC

Citation for the original published paper (version of record):

Hidalgo, S., Battaglia, J., Arellano, S. et al (2018). Evolution of the 2015 Cotopaxi Eruption Revealed by Combined Geochemical & Seismic Observations. *Geochemistry, Geophysics, Geosystems*, 19(7): 2087-2108. <http://dx.doi.org/10.1029/2018GC007514>

N.B. When citing this work, cite the original published paper.



Geochemistry, Geophysics, Geosystems

RESEARCH ARTICLE

10.1029/2018GC007514

Key Points:

- Multiparametric study of Cotopaxi 2015 unrest and eruption revealed an interaction between a magma intrusion and the hydrothermal system
- Remote measurements of SO₂, BrO, HCl, and CO₂ revealed a magmatic signature for the Cotopaxi gas plume during unrest and eruption
- A very small fraction of the theoretical degassing magma was emitted during the 2015 Cotopaxi eruptive phase

Correspondence to:

S. Hidalgo,
shidalgo@igepon.edu.ec

Citation:

Hidalgo, S., Battaglia, J., Arellano, S., Sierra, D., Bernard, B., Parra, R., et al. (2018). Evolution of the 2015 Cotopaxi eruption revealed by combined geochemical and seismic observations. *Geochemistry, Geophysics, Geosystems*, 19, 2087–2108. <https://doi.org/10.1029/2018GC007514>

Received 28 FEB 2018

Accepted 30 APR 2018

Accepted article online 7 JUN 2018

Published online 16 JUL 2018

Evolution of the 2015 Cotopaxi Eruption Revealed by Combined Geochemical and Seismic Observations

Silvana Hidalgo¹ , Jean Battaglia², Santiago Arellano³ , Daniel Sierra¹, Benjamin Bernard¹ , René Parra⁴, Peter Kelly⁵, Florian Dinger^{6,7}, Charlotte Barrington⁸, and Pablo Samaniego²

¹Instituto Geofísico, Escuela Politécnica Nacional, Quito, Ecuador, ²Université Clermont Auvergne, CNRS, IRD, OPGC, Laboratoire Magmas et Volcans, Clermont-Ferrand, France, ³Department of Space, Earth and Environment, Chalmers University of Technology, Göteborg, Sweden, ⁴Instituto de Simulación Computacional, Colegio de Ciencias e Ingenierías, Universidad San Francisco de Quito, Quito, Ecuador, ⁵Cascades Volcano Observatory, Volcano Science Center, U.S. Geological Survey, Vancouver, WA, USA, ⁶Max-Planck Institute for Chemistry, Mainz, Germany, ⁷Institute of Environmental Physics, University of Heidelberg, Heidelberg, Germany, ⁸Earth Observatory of Singapore, Nanyang Technological University, Singapore

Abstract Through integration of multiple data streams to monitor volcanic unrest scientists are able to make more robust eruption forecast and to obtain a more holistic interpretation of volcanic systems. We examined gas emission and gas geochemistry and seismic and petrologic data recorded during the 2015 unrest of Cotopaxi (Ecuador) in order to decipher the origin and temporal evolution of this eruption. Identification of families of similar seismic events and the use of seismic amplitude ratios reveals temporal changes in volcanic processes. SO₂ (300 to 24,000 t/d), BrO/SO₂ ($5\text{--}10 \times 10^{-5}$), SO₂/HCl (5.8 ± 4.8 and 6.6 ± 3.0), and CO₂/SO₂ (0.6 to 2.1) measured throughout the eruption indicate a shallow magmatic source. Bulk ash and glass chemistry indicate a homogenous andesitic (SiO₂ wt % = 56.94 ± 0.25) magma having undergone extensive S-exsolution and degassing during ascent. These data lead us to interpret this eruption as a magma intrusion and ascend to shallow levels. The intrusion progressively interacted with the hydrothermal system, boiled off water, and produced hydromagmatic explosions. A small volume of this intrusion continued to fragment and produced episodic ash emissions until it was sufficiently degassed and rheologically stiff. Based on the 470 kt of measured SO₂ we estimate that $\sim 65.3 \times 10^6$ m³ of magma were required to supply the emitted gases. This volume exceeds the volume of erupted juvenile material by a factor of 50. This result emphasizes the importance of careful monitoring of Cotopaxi to identify the intrusion of a new batch of magma, which could rejuvenate the nonerupted material.

1. Introduction

Cotopaxi volcano (5,897 m) is located on the western side of the Cordillera Real of Ecuador, 50 km south of Quito (Figure 1a). This volcano has a long eruptive history with more than 70 eruptions with an estimated volcanic explosivity index (VEI) between 2 and 4 since 1534 (Mothes et al., 2004). Eight of these eruptions are cataloged as VEI 4. Since the last deadly eruption in 1877, several smaller episodes of activity have occasionally been reported. The most remarkable were those of 1903–1906, when tephra fallouts, pyroclastic and lava flows, and lahars were generated (Pistolesi et al., 2011); and the reported activity of 1942, characterized by steam and ash emissions. Historical records indicate that prior activity has consisted of clusters of eruptive events separated by periods of long quiescence (months to years). Eruption clusters might start with mild events but are followed by increasing magnitude eruptions. The most dangerous hazards associated with this volcano are the devastating lahars that have been generated by sudden glacier melting during pyroclastic flow-forming eruptions (Hall & Mothes, 2008). In consideration of this hazard and given the recent population growth within the potentially hazardous zones, now exceeding hundreds of thousands of people, the Cotopaxi monitoring network has grown significantly since the installation of the first seismic station in 1976. At the time of writing (April 2018) the Instituto Geofísico of the Escuela Politécnica Nacional (IG-EPN) operates 59 different real-time monitoring instruments around the volcano (www.igepon.edu.ec).

Cotopaxi experienced unrest in 2001–2002, when anomalous seismicity and ground displacement were recorded (Hickey et al., 2015; Molina et al., 2008). These signals did not culminate in an eruption but were

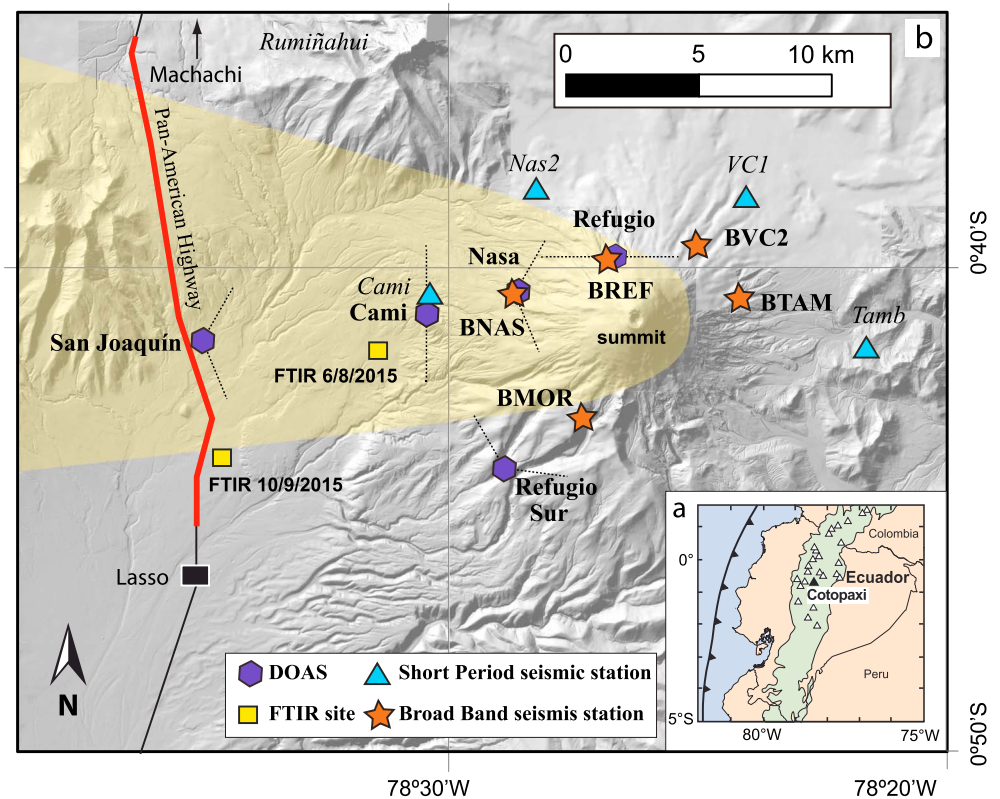


Figure 1. Location map of Cotopaxi and monitoring networks that provided data for this study. (a) Location of Cotopaxi Volcano in Ecuador. The green area outlines the approximate limit of the Andean mountain range. (b) Location of the broadband and short-period seismic stations and differential optical absorption spectroscopy (DOAS) instruments used in this study. Sites from where FTIR (Fourier-Transform Infrared spectroscopy) measurements were performed are also shown with their corresponding date. The Pan-American highway is shown in black color to the west of Cotopaxi. The typical length of DOAS traverses performed over this road is shown in red. Plume dispersion is shaded in yellow.

interpreted as the result of a magmatic intrusion with a low supply rate that stalled beneath the surface. Sporadic SO_2 emissions, 76 to 481 t/d, were also observed in 2009 (Bourquin et al., 2009) occasionally associated with an increase in the number of long-period seismic events (LPs) up to 93 events per day. Small seismic crises, mainly increased LPs numbers, were also observed in 2010 and 2011. Fumarolic activity was limited to the crater area and only sporadically, an active fumarole was observed on the upper western flank of the volcano. SO_2 emissions were very low and typically at the detection limit. The 2015 unrest phase began in April 2015 with preeruptive activity characterized by an elevated LP activity, SO_2 degassing and the appearance of tremor, lasting until 14 August 2015, when four hydromagmatic explosions initiated a new eruptive period. Geophysical parameters have been evaluated throughout the unrest and eruptive period (Global Volcanism Program, 2015 weekly reports; IG-EPN special reports, www.igepn.edu.ec). Surface activity started with gas emission in mid-May 2015. Ash emissions began after the 14 August explosions. The activity faded out at the end of November 2015. Small secondary lahars triggered by rainfall were produced since August 2015, affecting the main road in the Cotopaxi National Park. No primary lahars, lava, or pyroclastic flows were generated during this period.

Several authors have studied the 2015 unrest and eruptive period. The deformation pattern observed in the months before the eruption is described and modeled by Morales Rivera et al. (2017). These authors concluded that this deformation could be modeled by an opening volume of $6.8 \times 10^6 \text{ m}^3$ between 5.5 and to 12.1 km below the summit. Mass, distribution, and characteristics of the emitted volcanic products are described in Bernard et al. (2016) and Gaunt et al. (2016). Ash componentry evaluated by Gaunt et al. (2016) throughout the eruptive period shows significant changes with juvenile content (including free crystals) increasing rapidly after a few days of eruption from around 26% to 72–84%. On the contrary,

hydrothermal components that were up to 47% during the first explosions decreased to 4–15% at the end of the eruptive period. Gaunt et al. (2016) attributed this change to a progressive clearing of the magma ascent path and reduction of the interaction with the host country rock. Simultaneously, these authors observed an increase in the crystallinity of juvenile fragments indicating a slower ascent and/or longer residence times at shallow levels. Based on the evaluation of geophysical parameters such as the ash fallout mass and the seismic activity, as well as the eruptive character, Bernard et al. (2016) defined four phases inside this eruptive period. The first phase lasted only 2 days (14–15 August) and was characterized by the hydromagmatic explosions. The other three phases (15 August to 2 October, 2 October to 4 November, and 4 to 30 November) displayed a decreasing intensity and were dominated by an ash venting process driven by a high gas flux ($3,075 \pm 2,691$ t/d) and associated with intense seismic tremor. According to these authors, the total magnitude of the eruption was 2.1, based on the Pyle (2015) classification. The relationship between ash emissions and seismic tremor explored by Bernard et al. (2016) yielded two hypotheses for the origin of the recorded preeruptive tremor: (a) deep fragmentation of magma in a clogged conduit taking place before the system opened and (b) boiling off of the hydrothermal system due to a magmatic intrusion ultimately leading to hydromagmatic fragmentation. Early determination of which process is reflected by tremor would improve the understanding of the behavior of volcanic systems and enhance the IG-EPN monitoring capabilities.

In this contribution we characterize the composition and flux of multiple volatile species obtained by several methods, categorize the seismicity observed during the preeruptive phase (April–August 2015) and eruptive period (August–November 2015) and determine the petrological characteristics of the erupted material. By combining geochemical and geophysical information obtained for a prolonged period of time we clarify the overall picture of the evolution of activity.

2. Methods

2.1. Gas Emission

Sulfur dioxide (SO₂) has been measured at Cotopaxi since 2008 by two permanent scanning differential optical absorption spectroscopy (DOAS) stations located 2.5 km to the north (station Refugio-flat scanner) and 5 km to the west (station Nasa-conic scanner) of the crater (Figure 1). Flat or conic terminologies for scanning devices refer to the shape of the scanned surface as described in Galle et al. (2010). These are standard instruments from the Network of Observation of Volcanic and Atmospheric Change (NOVAC) project (Galle et al., 2010; Hidalgo et al., 2015). They provide constraints on SO₂ flux and plume location during daylight hours with a typical time resolution of about 10 min. Due to intense ash fallout after the onset of the eruptive activity, the Nasa station stopped working on 31 August. On 9 September, it was relocated to the San Joaquín site, 15 km to the west of the crater (Figure 1b), in the prevalent wind direction in Cotopaxi area. Two additional stations were installed on 24 and 26 September in order to improve the azimuthal coverage of the plume. A conic scanner was installed at Refugio Sur, 7.5 km to the south, and a flat scanner was installed at Cami, 7.5 km to the west of the crater (Figure 1b). On 27 September, we also changed the flat scanner at Refugio for a conic one in order to allow this station to see the plume drifting mainly to the west. Additionally, 136 mobile-DOAS traversers (four to eight per day) were conducted from 24 August to 12 December 2015, driving from Machachi to Lasso through the Pan-American highway (Figure 1b). This allowed us to complement the recordings during days when the permanent stations were down due to ash fallout or when significant ash was present. It is known that optically thick media, especially condensed and ash-laden plumes, affect the measurement of volcanic gas column densities, because the assumption of straight optical path through the entire plume may be severely compromised (e.g., Kern et al., 2010; Millán, 1980; Mori et al., 2006). Our distal mobile-DOAS traverses were less affected by these phenomena as they were performed 16 km from the vent where ash concentration was already low.

We processed data acquired by the permanent DOAS stations using the NOVAC software (Galle et al., 2010) in order to derive the daily mass emission of SO₂ in tons per day (t/d). We calculated the SO₂ fluxes using the slant column densities (ppm-m) measured by the network in combination with wind speed, wind direction, and plume height data. In order to get the most accurate estimation of the wind speed and direction we simulated meteorologic data for 2015 using the Weather Research and Forecasting (WRF V3.2) model (Michalakes et al., 2005; Skamarock et al., 2005). WRF is a last-generation Eulerian nonhydrostatic model used for meteorological forecasting and weather research. It is a fully compressible model that solves

the equations of atmospheric motion, with applicability to global, mesoscale, regional, and local scales. The meteorological simulations used a master domain of 80×80 cells (each of 36×36 km) and two nested subdomains, the second of which covers Ecuador with 199×199 cells (4-km horizontal resolution) and 35 vertical levels (1-km vertical resolution, the model top pressure is at 50 hPa, approximately 22 km above the ground). Initial and driving boundary conditions came from the National Centers for Environmental Prediction of the Department of Energy Reanalysis 2 Project (NCEP/DOE R2) with data provided by the Physical Sciences Division of the Earth System Research Laboratory of the National Oceanic and Atmospheric Administration (NOAA/ESRL PSD). This model has been used to model plume dispersion and deposition at Tungurahua volcano for the 2012, 2013, and 2014 eruptions (Parra et al., 2016). For each day, wind speed and direction were calculated at different levels (1- to 15-km altitude), at 1-hr intervals, over Nasa station using the horizontal wind components provided by WRF. When plume heights and directions were obtained by triangulation between two DOAS stations with a view of the plume at about the same time (Johansson et al., 2009), we used only wind speed from the WRF simulations. When no triangulation was possible, we used a standard altitude of 500 m above the crater level for the plume height and the corresponding plume direction and wind speed provided by the simulations. The choice of this standard plume altitude was supported by statistics on the measured values and visual observations obtained from continuous images taken from web cameras looking at the volcano (Bernard et al., 2016).

SO₂ emissions are presented in two different ways: as “extrapolated” and “observed” daily masses. Each permanent DOAS instrument provided 40 to 140 scans per day. Valid scans are those in which SO₂ is measured (good spectroscopic fitting; see Galle et al., 2010 for details) and plume completeness is higher than 0.5 (an empirical measure of how well the scan captures the entire plume; Johansson, 2009). The number of valid scans is highly variable (between 0 and 120), depending on weather conditions, amount of ash in the atmosphere, plume direction, and SO₂ content in the plume. The extrapolated daily mass is the highest station-specific average of all valid measurements during a day, extrapolated over 24 hr independently of the number of measurements. This procedure assumes that SO₂ emission is more-or-less constant and continuous during the whole day, and hence, the average value could be considered as representative of the daily emission. In contrast, the observed daily mass is the time integral of all valid measurements obtained during the day, where the highest value among the different stations during short time intervals is selected to represent each measurement (Hidalgo et al., 2015). This procedure takes into account the variations and the potential absence of SO₂ emission during the measurement period. The observed mass is expressed in tons per 10 hr (daylight hours at Cotopaxi latitude) and is multiplied by 2.4 to be compared with the extrapolated daily mass. The daily-validated measurement duration (DVMD) quantifies the total duration (expressed in minutes) of valid scans, and it has proved to be an efficient tool for identifying the presence of SO₂ emission (Hidalgo et al., 2015). Usually Nasa, Cami, or San Joaquín station detected the highest number of valid measurements and higher SO₂ values due to their location below the plume. Whenever these stations were down, the daily-observed mass was underestimated. During periods of activity with high and continuous SO₂ outgassing, the two methods yield fairly equivalent results.

For the Mobile DOAS traverses we used a system consisting of a mini-USB2000 Ocean Optics spectrometer coupled to a zenith-viewing telescope by a quartz fiber. To acquire and process the spectra we used the Mobile-DOAS v.5 software by Zhang and Johansson (2009). An external Global Positioning System (GPS) antenna provides precise location and time in order to calculate the integral SO₂ column amount across the section of the plume. Mobile DOAS data were processed using the same source of wind velocity as for the processing of data from the permanent stations. Wind direction was deduced directly from the traverse. Plume height was only used indirectly to retrieve the wind speed. Completeness of the plume was assured for all the traverses with plume widths varying from 1,200 to 13,000 m. Traverses typically gave higher columns than scanning measurements during the last days of August and the first days of September, due to the absence of the Nasa station to the West of the volcano and/or due to the intense ash fallout over the flanks where the permanent stations are installed. After the relocation of Nasa station to San Joaquin and the progressive decrease of ash content in the plume, the fluxes obtained by Mobile DOAS overall coincided with those provided by the permanent stations.

Bromine oxide (BrO) was also quantified from scan measurements following the method described in Lübcke et al. (2014). This calculation provided daily estimates of the BrO/SO₂ molar ratio (Dinger et al., 2018).

Nevertheless, some gaps in data are present due to the low quality of the scans from permanent stations given the high ash content in the plume (Dinger et al., 2018).

Additionally, nine airborne Multi-GAS (Multi-component Gas Analyzer System) measurement campaigns were performed using fixed-wing aircraft between late August and December 2015. These measurements were made using a Multi-GAS equipped with sensors to measure the following parameters at 1 Hz: H₂O and CO₂ (Licor 840A), SO₂ (City Technology Ltd., EZT3ST/F), H₂S (City Technology Ltd., EZT3H), GPS coordinates, ambient temperature and relative humidity (Vaisala HMP-60), ambient pressure, and diagnostic parameters. This instrument follows the approach of Aiuppa et al. (2007) and Shinohara et al. (2008). The specific instrument setup has been described in Gunawan et al. (2017).

Two solar FTIR (Fourier-Transform Infrared spectroscopy) campaigns were performed on 6 August and 10 September 2015 in order to measure SO₂/HCl ratios. For this, we used a MIDAC M4400 Series instrument with a sterling-cooled mercury-cadmium-telluride (MCT) detector, field of view of 30 mrad and a maximum resolution of 0.5 cm⁻¹. Solar spectra in the direction of the plume were acquired manually by scanning the direct solar beam with a flat Au-coated mirror. Measurements were made from below the gas plume at 7- and 15-km distance from the crater, respectively (Figure 1b). A total of 176 and 851 spectra were collected during the two campaigns from which only 7 and 10 spectra respectively showed simultaneous detection of SO₂ and HCl providing SO₂/HCl ratios. Spectra were acquired using MIDAC's Autoquant software and later processed with the MALT program using a three-layer model representing the plume and the background and foreground atmosphere above and below the plume. The model initializes with a standard tropical atmosphere composition and fits the effective concentrations of H₂O, N₂O, and CH₄, as well as those of the volcanic species SO₂ and HCl. The model includes fitting parameters for the effective temperature and pressure of each layer and instrumental parameters such as the field of view, effective apodization, or asymmetry of the line-shape. SO₂ was evaluated in the spectral range between 2,470 and 2,535 cm⁻¹ and HCl between 2,810 and 2,870 cm⁻¹, using the procedure described in Griffith (1996).

2.2. Seismicity

The permanent seismic monitoring network of the IG-EPN around Cotopaxi includes five broadband three-component and five short period one-component stations (Figure 1b) sampled at 50 and 100 Hz, respectively. We examined several parameters to quantify both short- and long-duration seismic signals related to volcanic activity. For this purpose, we mainly used the continuous recordings from the vertical component of station BREF, a three-component broadband sensor that is the closest to the summit (Figure 1b) and for which recordings are the least influenced by anthropogenic noise or external sources such as lahars. BTAM was also used for calculating amplitude ratios, as explained below, and all available stations were used for the visual inspection of signals.

First, to quantify the amplitude of long-term processes, such as tremor, we calculated median seismic amplitudes (MSA) over 10-min sliding windows (without overlap) after filtering the seismic signals between 0.5 and 5 Hz, which is the main frequency band for signals related to venting processes (Figure 2a). To determine the median value of each 10-min window, we filtered the seismic signal with a four-pole Butterworth filter, calculated the absolute value of the seismic amplitudes, and determined the median value of the amplitude distribution. We used the median amplitude because it is less influenced by transient events as compared to the root mean square amplitude. All amplitudes are expressed in physical values (μm/s) after correcting the raw amplitudes for the gain of the station.

Second, to count the transient events (i.e., any type of short-lived seismic signal), we applied an automatic STA/LTA (short-term amplitude/long-term amplitude) algorithm. To detect all types of transients, including low-frequency/long-period (LP) events as well as high-frequency volcano tectonic (VT) events, the algorithm was applied to data filtered between 1 and 22 Hz with a two-pole Butterworth filter. These frequencies almost cover the full short-period frequency range provided by the instrument. We used an LTA of 20 s and an STA of 0.5 s and considered a minimum delay between two successive events of 7 s to avoid double counting the events (Figure 2b). For each detected transient, we calculated the peak-to-peak amplitude in a four-second window around the detection time (Figure 2c). The number of detected events depends on the STA/LTA threshold. For a low threshold of 2.5, the majority of events are very small with about 60% of them having amplitudes below 1.65 μm/s (800 counts) during year 2015 and 70% during the period 2013–2015. We

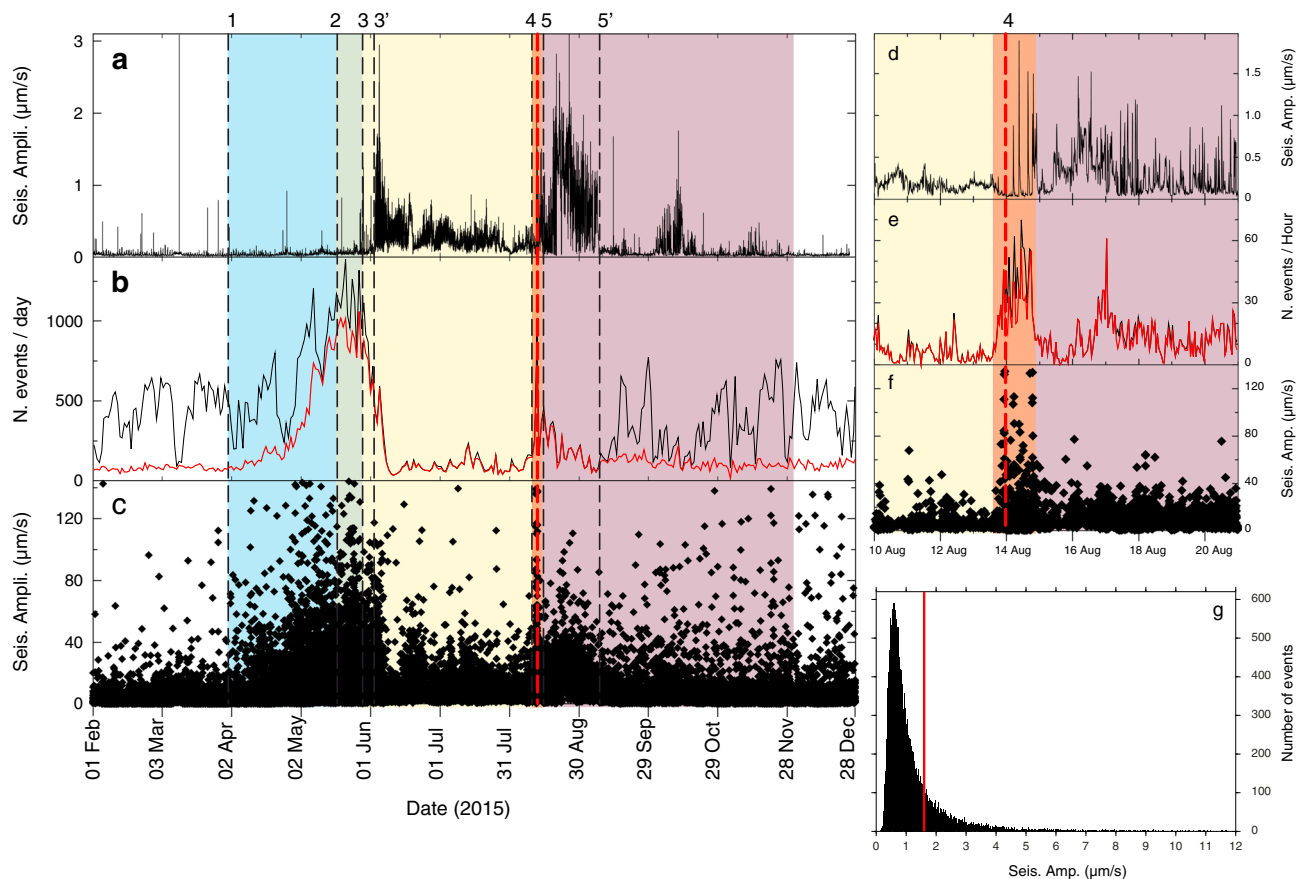


Figure 2. Time series of seismicity at Cotopaxi during 2015. The background colors indicate the eruptive phases defined in the text. Numbers at the top of the black dashed lines indicate important dates at the beginning or within these phases. 1: 1 April, 2: 19 May, 3: 30 May, 3': 4 June, 4: 13 August, 5: 15 August, 5': 11 September. Red line represents the hydromagmatic explosions of 14 August. (a) Median seismic amplitude calculated over 10-min sliding windows (without overlap) after filtering the signal between 0.5 and 5 Hz. (b) Number of transient events per day with an STA/LTA (short-term amplitude/long-term amplitude) higher than 2.5 (black) and with a peak-to-peak amplitude higher than 1.65 $\mu\text{m/s}$ (red). (c) Peak-to-peak amplitude, calculated between 1 and 22 Hz, of the individual seismic events with an STA/LTA higher than 2.5. (d–f) 10–21 August data as in (a)–(c). In (e) STA/LTA counting is in events per hour. (g) Histogram of peak-to-peak amplitudes of transient events with an STA/LTA higher than 2.5. The red line shows the 1.65- $\mu\text{m/s}$ arbitrary limit used to avoid including persistent background events.

present the total number of events for an STA/LTA threshold of 2.5, as well as the subset of larger detected events having additionally a peak-to-peak amplitude above 1.65 $\mu\text{m/s}$ (800 counts; Figure 2b). This amplitude threshold was arbitrarily set to eliminate the large peak of small events (primarily detected on BREF station) visible on the histogram of event amplitudes (Figure 2e).

Transient events detected at Cotopaxi include VT and LP events, explosion quakes, and various types of events related to venting processes, but also ice quakes (IQs) with various spectral signatures related to the presence of a glacier covering the summit of the volcano (Métaxian et al., 2003). IQs have various origins including fracture propagation or opening, collapse of ice blocks, basal friction, or water circulation (Helmstetter et al., 2015; Podolsky & Walter, 2016). In this last case, they may have similar spectral signatures and possibly also similar source mechanisms as some magmatic events, related to crack-fluid resonances (Métaxian et al., 2003; Weaver & Malone, 1976). IQs may be confused with LPs and VTs because of sometimes comparable spectral and waveform characteristics. An event-per-event exhaustive identification is, however, impossible because of the very large number of detected events. The wide range of signals, with variable and sometimes similar spectral characteristics, makes the identification complex. For this reason, we did not use the preliminary catalog resulting from daily monitoring (Gaunt et al., 2016; Morales Rivera et al., 2017; Mothes et al., 2017), which is mostly based on visual identification of waveforms at a single reference station and may unfortunately include significant numbers of misidentifications. Therefore, to identify the different types of events activated prior to and during the eruption, we chose an approach based on the automated

waveform search of families of repeating events. Each family is typically representative of a given source process and mechanism. Such families are commonly observed on volcanoes for all categories of events and are characteristic of different periods of activity during an eruption (e.g., Green & Neuberg, 2006; Rodgers et al., 2016).

To identify the families that were active at Cotopaxi between January 2013 and the end of November 2015, we used cross correlation to classify the events detected by our STA/LTA algorithm, similar to the procedures used by Vallee et al. (2013) and Battaglia et al. (2016). We selected all events with an STA/LTA higher than 3.5 for 2013 and 2014 and all higher than 3.0 for 2015. These relatively low detection thresholds allow the processing of small amplitude events but also include noise transients that are disregarded later in the processing. Our processing identified 45,426 events for 2013; 36,400 for 2014; and 59,460 for 2015. For these 141,286 events, we extracted for the vertical component of BREF station 1,024-sample (20.48 s) signal windows, starting 300 samples (6 s) before the triggering time. Classifications were done by comparing all events to each other using cross correlation after filtering between 1 and 8 Hz. Empirically, we found that these rather low-frequency filtering parameters provided meaningful classification results compared to higher-frequency ones. We considered that an event belongs to a family if it has a correlation coefficient higher than a given threshold (from 0.70 to 0.85) with at least one of the other family events. This type of classification corresponds to open clusters allowing chain similarity (Battaglia et al., 2016).

Because of the high number of selected events (141,286), we could not compare all events to each in a single run. Therefore, we used a two-stage process. First, we did preliminary classifications, involving up to 40,000 events at a time, for various time periods and detection thresholds. We considered short time frames (month) including small detected events as well as longer time frames including mostly larger events. This procedure allowed the identification of families involving larger events, long-lasting families, and families including mostly small events. Secondly, to summarize and group results, we selected all events included into the preliminary families of more than five events obtained for a low threshold of 0.70 and merged these events into a single run including 48,004 events. Hereafter, we mostly discuss families obtained for a threshold of 0.85 (named xyz. 85) or 0.80 (named xyz. 80) for events including more high frequencies such as VTs since their similarity is lower for the same band-pass filtering.

We first examined the temporal evolution of families to identify characteristic temporal patterns. To identify the type of events involved in each family, we visually examined waveforms at the 10 stations located around the volcano. We also calculated ratios of peak to peak amplitudes between the closest station and the summit (BREF, 2.4 km from the summit) and a more distant one (BTAM, 4.5 km) and examined their histograms for each family. These ratios may be a proxy for the source depth (Battaglia et al., 2016) as long as the sources are located below the summit area. Finally, for some selected smaller families (including fewer events), we stacked similar waveforms to build templates and used them for matched filtering detection. Then, we defined all events with a correlation higher than 0.70 as similar to the reference templates. This procedure allowed us to identify more events and therefore complement the families and provide more complete temporal evolutions. This procedure was not applied to larger families, extending over long durations, in which chain similarity plays a significant role. For these families the use of a single template for matched filtering does not allow identifying more events than the classification into families (open clusters).

2.3. Bulk Ash, Glass, and Microlite Compositions

In order to gain insights into the juvenile magma composition and the preeruptive conditions, ash samples were initially collected from solar panels on 14–15 August. Then we used ashmeters (Bernard, 2013) to collect samples from the following phases, and we include here the analyses of representative dates (see below). Samples were dried at 40°C for over 24 hr and prepared for the different analyses. Bulk ash was analyzed for major elements for six samples corresponding to 14 August (2), 24 August (1), 28 August (1), and 20 October (2) at the Departamento de Metalurgia Extractiva of the Escuela Politécnica Nacional by X-ray fluorescence using a Bruker S8 Tiger instrument. Analytical errors are less than $\pm 1\%$. Dates were chosen in order to track potential changes in the composition between ash emitted just after the hydromagmatic explosions and ash corresponding to the ash venting episodes defined by Bernard et al. (2016). Glass and microlite were analyzed for major element compositions at the Laboratoire Magmas et Volcans of the University Clermont-Auvergne, using an electron microprobe CAMECA-Camebax SX-100, operating at 15-kV accelerating voltage,

and using a beam current of 15 nA for mineral analyses and 8 nA and a 5- μm defocused beam for glass analyses. The estimated error for a single analysis is approximately 1% when the element concentration is higher than 10% and of 2–5% when it is lower than 10%. S, F, and Cl were also analyzed in the matrix glasses. No melt inclusions were found in phenocrysts preventing the analysis of initial volatile concentrations at melt entrapment depths. Data are shown in Table 1.

3. Results

3.1. Seismicity

3.1.1. Overview of Seismic Parameters

The time series of seismicity shown in Figure 2 outlines several interesting features and provides a timeline of the eruption. The nature of the observed transient events is discussed according to the results from the classification scheme detailed above. During the initial months of 2015, as well as during the preceding years (see Figure 4), the number of transient events detected over the background level was relatively high. This permanent background seismicity mostly includes weak events, which are interpreted hereafter as being mostly IQ related to the dynamics of the large glacier covering the summit of the volcano. In this section, we disregard these events and comment on the number of larger events with a peak-to-peak amplitude above 1.65 $\mu\text{m/s}$ (800 counts), as explained above.

Starting in early April 2015, the number of large events increased considerably (Figures 2b and 2c). These events were identified mostly as preeruptive LPs. They peaked in both number and amplitude by mid-May when SO_2 surpassed the background level established since 2008 (Figure 5). On 4 June, the activity shifted from a predominance of LPs to preeruptive tremor, as evidenced by the sharp increase in the MSA (Figure 2a). However, we note that, in contrast to observations at other volcanoes (e.g., Neuberg et al., 2000), this shift does not correspond to LPs occurring at an accelerating rate and merging into tremor. The number of detected events then quickly dropped on 4 June (Figure 2b) and remained at a relatively low level during the following weeks with only larger events being detected due to the presence of a high background noise. These signals were mostly LPs or transients related to venting processes. Tremor was at first composed of pulses, sometimes regularly spaced, and occasionally evolved toward continuous tremor during the following 2 months. This preeruptive tremor was mostly nonharmonic and broadband.

Starting in the afternoon of 13 August, the number of transients progressively increased, including events from several small families. These preceded and accompanied the major explosions on 14 August (Figure 2d). These events were followed by eruptive tremor with a strong increase of the MSA on 21 August (Figure 2a) and a progressive decay of the number of detected significant events (red curve in Figure 2b) until 11 September when their number stabilized. MSA sharply dropped also on 11 September, corresponding to the waning of the second phase of ash emission (Bernard et al., 2016). Subsequently, there was an increase in the number per day of small detected events (black curve in Figure 2b). The amount of larger events per day remained; however, steady and low, slightly above the pre-April 2015 level. The results of the classification of events based on the families' approach suggest that most of the transient events observed after 11 September were IQs. This also confirms observations of Bernard et al. (2016) indicating that post 14 August seismicity linked to eruptive activity includes mostly tremor. Finally, two additional tremor phases, associated with ash emissions, were observed with globally decreasing maxima and average amplitudes until the end of the eruptive activity in November, as described in Bernard et al. (2016).

3.1.2. Seismic Transients Recorded at Cotopaxi

The classification of transients detailed above includes, for a similarity threshold of 0.85, the presence of 427 families including more than 5 events, 90 including more than 20 events, and 5 with more than 1,000 events. Figure 3 shows examples of such families. Furthermore, we determined four characteristic types of temporal evolutions of the number of events in these families through time. Examples of these typical distributions are given in Figure 4.

The first and most common type of temporal evolution (type 1) corresponds to families that are not specifically related to the 2015 eruptive activity of Cotopaxi. In particular, several families in this type, including up to 6,600 events, are constantly active during the entire period 2013–2015, at a rather constant rate. Those families include events clearly observed at station BREF that commonly have very small amplitudes or are

Table 1

Major Oxides Compositions and LOI (Loss on Ignition) in wt % for Bulk Ash, Juvenile Glass, and Plagioclase Microlite for Cotopaxi Ash

Material	Analyze Code	SiO ₂	TiO ₂	Al ₂ O ₃	FeO _t	MnO	MgO	CaO	Na ₂ O	K ₂ O	Cr ₂ O ₃	P ₂ O ₅	LOI	Total
Matrix glass	70	65.54	1.00	13.14	6.41	0.22	1.02	2.86	4.18	3.73				98.10
	33	66.04	1.57	13.45	7.08	0.22	1.05	2.82	4.38	3.47				100.08
	34	66.68	1.14	13.06	6.51	0.04	0.93	2.89	3.31	2.86				97.43
	88	67.30	0.53	13.66	7.67		0.12	1.38	3.81	3.56				98.02
	27	70.75	0.77	12.44	3.75	0.05	0.30	1.11	2.40	3.58		0.01		95.18
	30	71.22	0.86	12.50	3.79	0.16	0.29	1.30	3.08	4.05		0.04		97.29
	28	71.29	0.88	12.59	3.56	0.14	0.27	1.19	2.28	3.77		0.00		95.99
	53	71.50	0.99	13.24	2.82	0.07	0.19	1.73	3.09	4.64		0.02		98.28
	31	71.67	0.77	12.76	3.49	0.07	0.40	1.04	2.58	3.51				96.29
	85	73.72	0.54	13.25	1.85		0.16	1.14	3.50	4.64				98.81
	64	64.93	1.34	13.78	6.04	0.10	1.24	3.48	3.73	3.51		0.01		98.76
	65	65.17	1.27	14.57	5.90	0.06	1.39	3.67	3.29	3.68		0.02		99.45
	66	64.21	1.34	12.05	8.33	0.20	3.66	3.78	2.90	3.07		0.03		99.86
	Gaunt et al. (2016)	63.60	1.30	14.30	7.40	0.20	1.60	4.30	3.20	3.50				98.65
	Gaunt et al. (2016)	66.40	1.20	13.50	7.60	0.10	1.10	2.50	3.90	3.00				96.82
	Gaunt et al. (2016)	63.40	1.30	14.10	7.90	0.10	1.60	4.30	3.50	3.10				97.00
	Gaunt et al. (2016)	64.20	1.30	14.50	6.70	0.00	1.90	4.40	3.80	2.60				97.52
	Gaunt et al. (2016)	64.20	1.20	14.30	7.20	0.20	1.90	4.90	3.30	2.10				96.88
	Gaunt et al. (2016)	64.70	1.20	14.50	7.60	0.10	1.60	4.00	3.30	2.30				97.12
	Gaunt et al. (2016)	65.80	1.30	13.70	6.20	0.00	1.60	3.50	2.50	4.90				97.70
Bulk ash	1–15 August 2015	52.6	0.82	16.09	6.72	0.11	2.58	6.69	3.3	1.18		0.23	7.83	90.32
	2–15 August 2015	54.48	0.84	16.55	6.64	0.12	2.6	6.17	3.36	1.21		0.23	6.53	92.2
	1–24 August 2015	56.63	0.86	17.96	7.18	0.18	3.58	7.00	3.95	1.29		0.24	0.4	98.87
	1–28 August 2015	56.54	0.86	17.61	7.33	0.19	3.85	7.03	4.01	1.32		0.24	0.04	98.98
	2–10 October 2015	57.47	0.84	17.99	7.11	0.19	3.58	6.79	4.07	1.35		0.21	0.02	99.6
	1–20 October 2015	55.33	0.83	17.19	6.98	0.18	3.54	6.69	3.94	1.32		0.21	0.01	96.21
		SiO ₂	TiO ₂	Al ₂ O ₃	FeO _t	MnO	MgO	CaO	Na ₂ O	K ₂ O	Cr ₂ O ₃			Total
Plagioclase microlite	29	62.43	0.13	22.26	1.14	0.00	0.04	5.66	7.31	1.50	0.00			100.47
	82	59.36	0.24	23.82	1.12	0.00	0.11	7.65	5.75	1.03	0.00			99.08
	83	60.77	0.14	24.71	1.09	0.05	0.05	7.28	5.92	0.95	0.00			100.96
	86	61.32	0.06	25.45	1.77	0.03	0.10	6.08	6.11	0.75	0.01			101.67
	90	59.02	0.02	24.64	0.76	0.01	0.04	7.88	6.16	1.11	0.08			99.64
	16	55.66	0.00	27.03	1.02	0.02	0.10	10.36	5.26	0.39	0.00			99.84
	60	56.80	0.00	25.40	0.90	0.00	0.00	8.82	5.58	0.76	0.01			98.26
	72	57.33	0.04	25.92	0.73	0.00	0.03	8.90	6.01	0.54				99.49
		Putirka (2008)						Waters and Lange (2015)						
	Low-silica glass	<i>T</i> (°C)	<i>P</i> (Mpa)	H ₂ O (wt%)	Depth (km)	H ₂ O (wt %)								
Initial <i>T</i> and <i>P</i>	950°C, 200 Mpa	1,055 ± 6	220 ± 97	0.99 ± 0.14	8.5 ± 3.6	2 ± 0.5								
Initial <i>T</i> and <i>P</i>	1,000°C, 400 Mpa	1,066 ± 6	244 ± 98	0.93 ± 0.14	9.4 ± 3.8	1.1 ± 0.5								
	High-silica glass													
Initial <i>T</i> and <i>P</i>	950°C, 200 Mpa	971 ± 6	1.34 ± 0.13		1.7 ± 0.17									
Initial <i>T</i> and <i>P</i>	1,000°C, 400 Mpa	981 ± 6	1.3 ± 0.14		0.8 ± 0.2									

not visible at the other stations. Amplitude ratios BREF/BTAM are typically widely spread around a value of ~10, corresponding to shallow sources. We consider these events to be IQs originating in the glacier that covers the summit of the volcano. This suggests that a large part the background seismicity corresponds to IQs. This seismicity was undetectable from June to August because of the presence of tremor and elevated background noise that prevented its detection. It reappeared in September when tremor diminished. Among these type-1 families, the third largest one differs from the others. It includes events that are clearly recorded at all stations of the network, mostly between mid-August 2013 and mid-March 2014. Its amplitude-ratio histogram also differs with a peak around 2.0–2.5, similarly to type-2 families detailed below, suggesting it groups LPs rather than IQs.

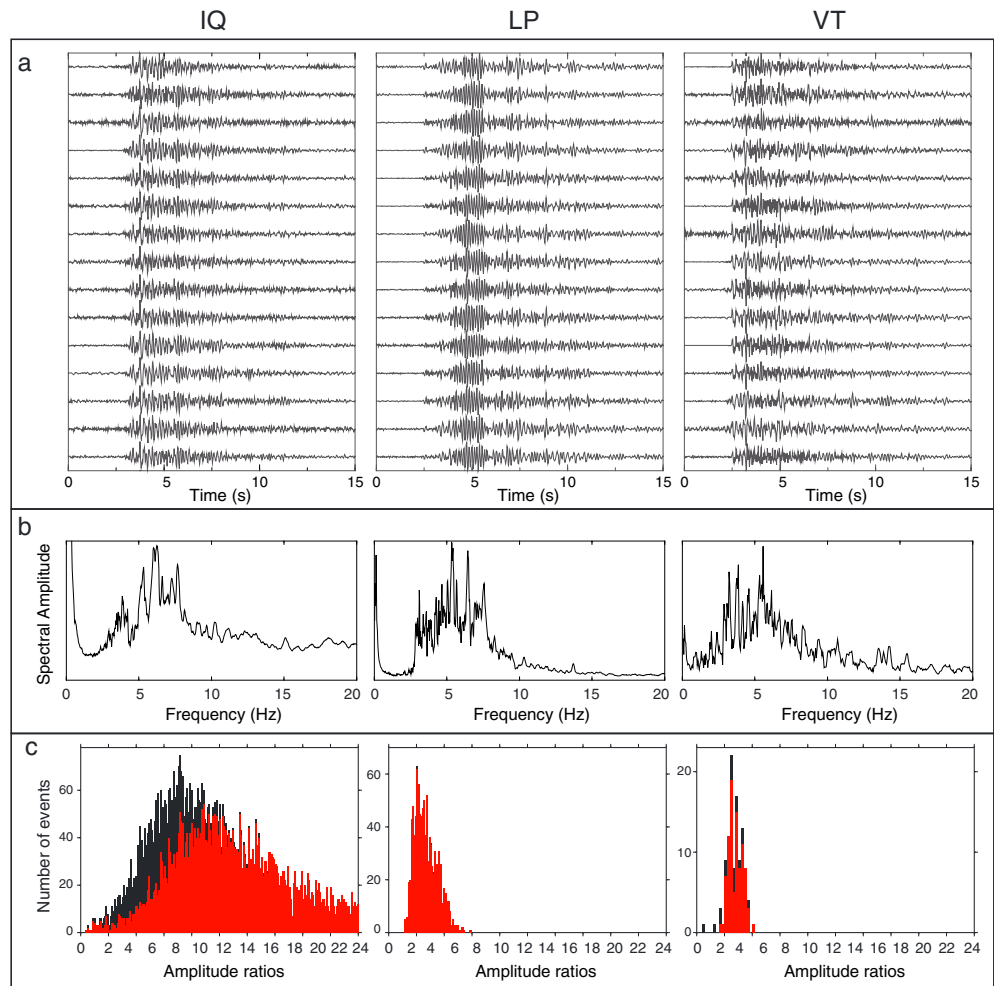


Figure 3. Examples of three families of similar events. (a) Normalized waveforms for a family of ice quakes (IQs; 001.85), long-period seismic events (LPs; 005.85), and volcano tectonic events (VTs; 030.80). (b) Respective average spectra for waveforms shown in plot a, corresponding to a summing of spectra of individual similar events. (c) Histograms of amplitude ratios between the amplitudes at stations BREF (2.4 km from the summit) and BTAM (4.5 km). Black histograms show all amplitude ratios, while red ones show amplitude ratios when amplitude at BREF is higher than 1.65 $\mu\text{m/s}$.

Type-2 families are active in April and May 2015 only. At correlation threshold 0.85, we identify several of them. All families included events that are well recorded by most of the stations and have amplitude-ratio histograms peaking around 2–3, suggesting sources with a reduced spatial extent at depths below the summit. These families include most of the larger events recorded during this period. Hereafter, we name these events LPs as they are directly related to the volcanic activity and lack clear P and S arrivals. However, we note that their spectral content, which peaks up to 5–7 Hz with little energy below 2.5 Hz, differs from LPs as defined by Chouet (1996).

Type-3 families are those mostly active on 13 and 14 August 2015, before and during the first hydromagmatic explosions. The classification of the detected events for August identifies a small number of families. At the correlation threshold of 0.80 we identify five families of VTs that are active on 13 and 14 August (030.80, 140.80, 268.80, and 395.80 in Figure 5). On 13 August, these families start their activity around 22h00 UTC, several hours before the first explosion at 09h02 on 14 August (Bernard et al., 2016). Their activity vanishes at 19h00, just after the third explosion mentioned by Bernard et al. (2016) on this same day. During this time, a total of 73 events were detected by matched filtering at a threshold of 0.70 and 144 at a threshold of 0.60. While proper locations could not be obtained at this point because of their small amplitude, these events appear to originate from below the summit at shallow depth (few kilometers). Additionally, we note the

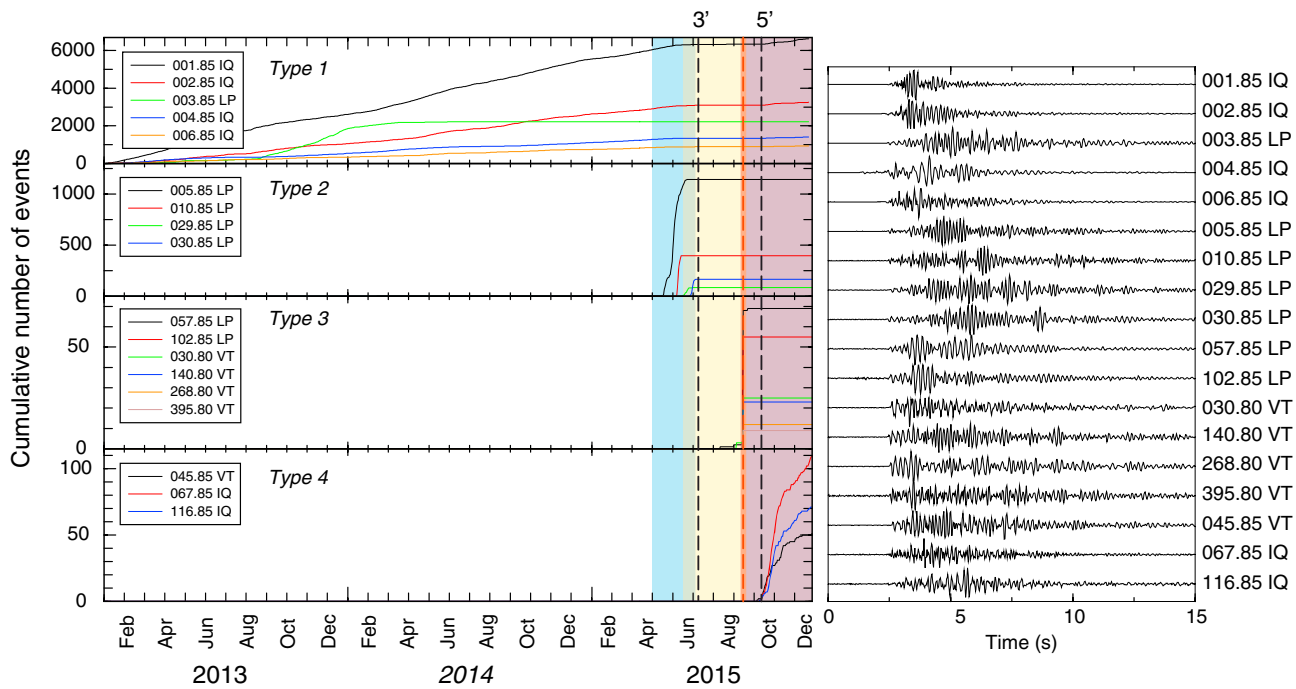


Figure 4. Characteristic temporal evolutions of families. Left plot: Examples of cumulative number of events for 18 families belonging to the four typical types of temporal evolutions. Color code is same as in Figure 2. The main period of tremor starts on 4 June (3') and ends on 11 September (5'). Red line indicates the hydromagmatic explosions on 14 August. Right plot: Stacked waveforms at station BREF for these 18 families. IQ = ice quake; LP = long-period seismic event; VT = volcano tectonic event.

presence during this same period of activity of at least two families (families 057.85 and 102.85 in Figure 5, for example) of LPs or events that may be related to venting processes.

Type-4 families correspond to new families starting after the drop in amplitude of the first episode of eruptive tremor on 11 September. These families mostly include small events with amplitude-ratio histograms similar to most of the type-1 families, suggesting these may be IQs. Only one of these families includes VTs with up to 54 events at the end of our study period (family 045.85 in Figure 4). At this time, type-1 families also reappeared due to the drop of tremor amplitude that allowed the detection of small events previously buried in the background noise. We note that these results are different from previous preliminary observations of high numbers of VTs (an average of 100 events per day) during this period (Gaunt et al., 2016; Morales Rivera et al., 2017; Mothes et al., 2017) since they rather indicate low numbers of VTs and the reappearance of IQs after 11 September.

3.2. Gas Emission

Background SO_2 emission at Cotopaxi before the 2015 unrest was around 27 ± 26 t/d measured typically during a DVMD of 52 ± 32 min. The first important change in SO_2 emission was detected on 19 May 2015, about 6 weeks after the increase in seismicity, and coincident with the peak in number and amplitude of the individual detected seismic events, identified as LPs (Figure 2b). The change in SO_2 appeared first as an increase in the number of automatic valid gas detections and, consequently in the DVMD reaching values of 368 ± 128 (± 1 s.d.) min indicating a shift from null or sporadic detectable emissions to more continuous detection of SO_2 (Figure 5a). In this period SO_2 fluxes slightly increased to 309 ± 290 t/d. On 30 May, the daily observed mass flux showed a more marked increase from the previous values to $1,310 \pm 973$ t/d, with, however, significant fluctuations of the emitted masses until 13 August (Figure 5b). After the hydromagmatic explosions of 14 August the SO_2 emission almost tripled, showing values of $3,127 \pm 2,688$ t/d until 30 November (Figure 5b).

The concentration of BrO retrieved from the spectra was above detection levels only after 4 June (Figure 5c). At this time BrO/ SO_2 molar ratios were very low ($6.27 \pm 8.79 \times 10^{-6}$) but the detection of BrO was coincident with the shift from individual seismic events to tremor. SO_2 emission remained at similar rates until the last days of July, after which both MSA and SO_2 showed a slight decrease, with SO_2 values averaging

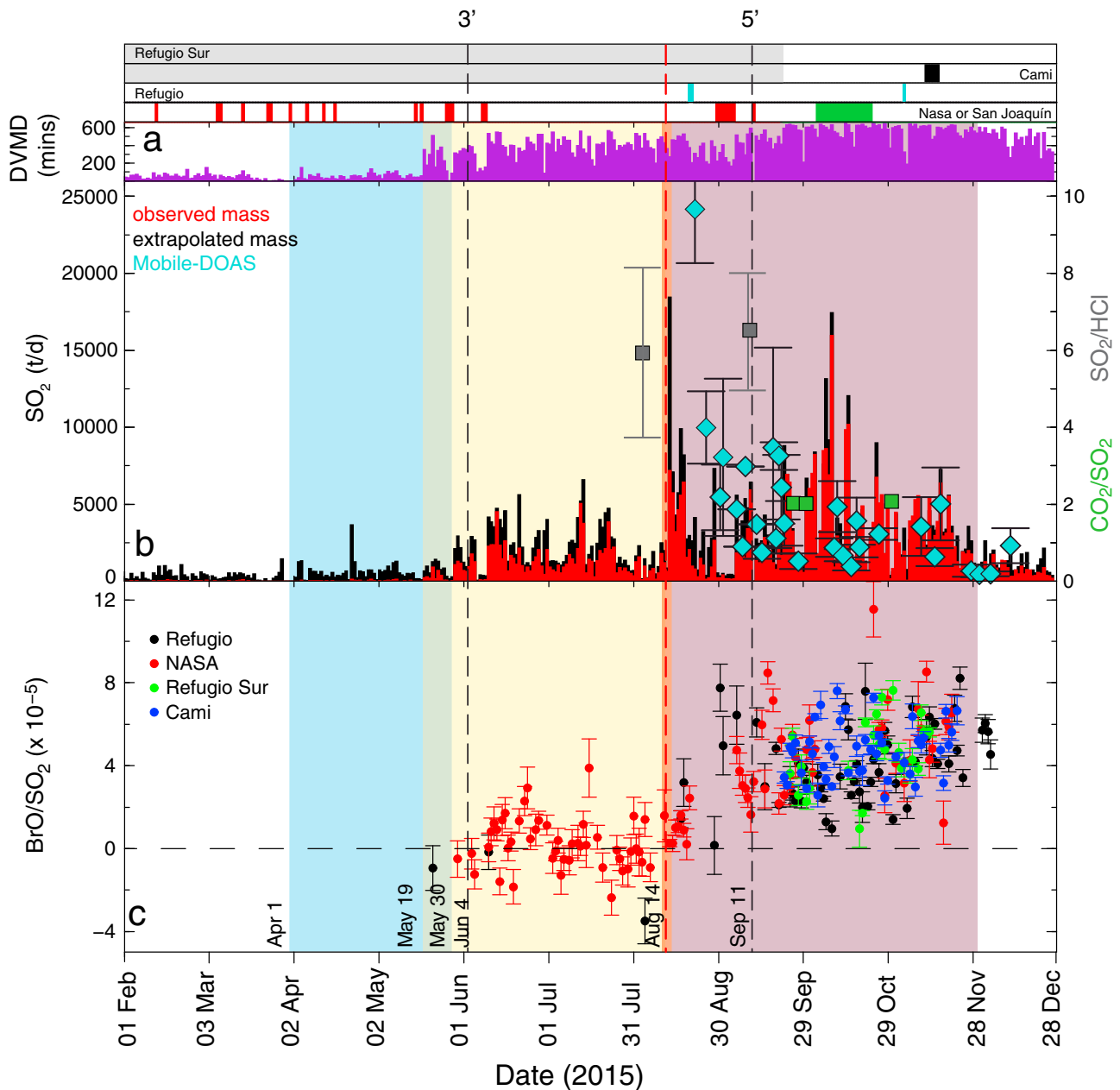


Figure 5. Degassing parameters measured at Cotopaxi during 2015. Background colors represent the previously defined phases as in Figure 2. The upper four cells are white whenever DOAS stations were functioning, and black, cyan, and red or green whenever Cami, Refugio, and Nasa or San Joaquin stations, respectively, were not working. Refugio Sur worked continuously since its installation. (a) Daily validated measurement duration (DVMD) of differential optical absorption spectroscopy (DOAS) gas emission data. (b) “Extrapolated” (black) and “observed” (red) SO_2 mass flux expressed in tons per day. Note that before the increase in the DVMD the extrapolated mass overestimates the emission, compared with the observed (red bars) whereas when DVMD is high (>400 min) both methods give similar results. Measurements obtained by DOAS traverses are shown as diamonds (cyan). Gray and green squares show the SO_2/HCl ratios obtained by FTIR and CO_2/SO_2 ratios obtained by MultiGAS, respectively. (c) BrO/SO_2 ratios measured by each of the four DOAS stations installed at Cotopaxi. Vertical dashed lines correspond to key dates in the evolution of Cotopaxi’s eruptive activity, 4 June (3’) and 11 September (5’). Red dotted line represents the hydromagmatic explosions on 14 August.

762 ± 476 t/d (27 July to 13 August) (Figures 2a and 5b). Then, on 14 August, four hydromagmatic explosions took place. The SO_2 mass associated with these explosions was calculated from Ozone Monitoring Instrument and Ozone Mapping and Profiler Suite data to be 17.51 and 12.52 kt, respectively (<http://so2.gsfc.nasa.gov/pix/daily>). Permanent stations were severely affected by ash during this day precluding good quality SO_2 measurements. On the next day, the SO_2 emission rate measured by the permanent stations increased to 18 kt/d. The highest value of SO_2 recorded by mobile DOAS was 24 kt/d on 24 August.

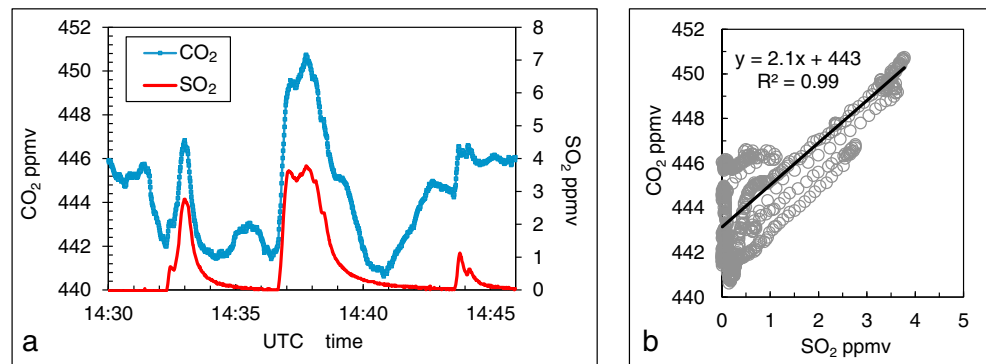


Figure 6. Example of airborne Multi-component Gas Analyzer System measurements. (a) CO₂ and SO₂ mixing ratios measured during three plume transects on 2 October 2015. (b) CO₂ versus SO₂ scatter plot for the measured transects with an example regression line shown for the transect with the highest measured CO₂ and SO₂ values. Note that the slopes of all the plume transects are generally consistent, despite the variable ambient CO₂ background.

After the 14 August explosions, BrO detection was reliable with BrO/SO₂ ratios around 3×10^{-5} that increased up to $5\text{--}10 \times 10^{-5}$ in the following days. On 21 September, SO₂ emissions peaked at 8.7 kt/d. SO₂ progressively decreased to a minimum of 1.2 kt/d on 30 September, followed by a progressive increase leading to a new peak of 16 kt/d on 12 October associated with renewed ash emissions described by Bernard et al. (2016). After the explosions BrO/SO₂ ratios showed a periodic pattern with a periodicity of 2 weeks (Dinger et al., 2018). These authors suggest that this pattern could be linked to Earth tides rather than to an eruption-induced control. By the end of November 2015, SO₂ emissions decreased to near-background levels and ash emissions and seismic tremor ceased. Finally, BrO detection became sporadic after December 2015.

A total of about 470-kt SO₂ was emitted by Cotopaxi between April and November 2015, of which approximately 106 kt (23%), was emitted before 14 August, when the four hydromagmatic explosions occurred.

The SO₂/HCl ratios measured by FTIR on 6 August and 10 September were 5.8 ± 4.8 and 6.6 ± 3.0 , respectively (Figure 5b). Hence, no major change was observed in the SO₂/HCl ratio before and after the hydromagmatic explosion of 14 August. These values are inside the field displayed by andesitic arc volcanoes, from 0.1 up to 24, but are above the average cluster of around 2 (Aiuppa, 2009). Together the FTIR and DOAS measurements independently showed that halogen-containing gases (HCl and BrO) were present in the plume before the 14 August explosions.

Airborne traverses primarily sampled the plume at distances ranging from ~3 to 8 km downwind and at altitudes of ~6,300 to 7,200 m above sea level. The high altitude of the plume and the relatively coarse analytical resolution of the Multi-GAS compared to sensitive airborne-specific instrumentation (e.g., Kelly et al., 2013) made plume composition measurements difficult. Also, the presence of an ash-rich plume prevented the airplane from completing direct plume traverses on several occasions. Nevertheless, during five out of the nine flights, low concentrations of SO₂ were detected (typically <1 ppmv) and during three of these flights (29 September, 2 October, and 6 November 2015), sufficient volcanic CO₂ (1 to 10 ppmv), and SO₂ (0.76 to 3.5 ppmv) were resolved above ambient background levels to calculate plume CO₂/SO₂ ratios. Volcanic H₂O could not be distinguished above ambient background and H₂S was not detected during any flight, indicating that SO₂ was the main S-containing gas in the plume. An example of an airborne plume transect is shown in Figure 6a. While the collected data were sparse, molar CO₂/SO₂ ratios calculated using the scatterplot method (e.g., Werner et al., 2013) were low (CO₂/SO₂ = 0.7 to 2.1, $r^2 = 0.68$ to 0.99; $n = 25$ to 117; Figure 6b) and similar to those found at other andesitic arc volcanoes that experience magmatic unrest and/or eruptions (Aiuppa et al., 2017).

3.3. Bulk Ash, Glass, and Microlite Equilibria

Bulk ash compositions for 14 August ash display a high LOI (loss on ignition), around 7%, confirming the presence of water and other volatiles or salts in this ash. These samples were particularly enriched in hydrothermally altered material and lithics, likely originating from the hydrothermal system and the conduit (Gaunt et al., 2016). Among the hydrothermally altered grains, the presence of pyrite, gypsum, anhydrite, and alunite is remarkable. The other four samples from 24 and 28 August and 20 October (two samples) show a homogeneous andesitic

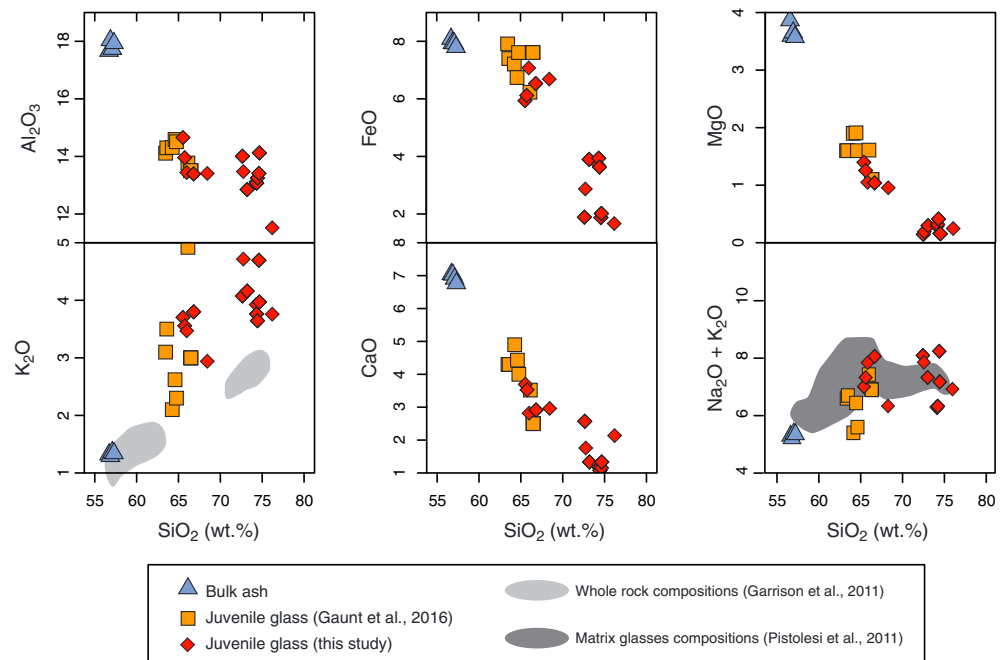


Figure 7. Harker diagrams for bulk ash and juvenile matrix glass from 2015 products. Juvenile glass compositions from Gaunt et al. (2016) are also included. The bulk ash compositions of 14 August samples are not shown as they cannot be considered as representative of the magmatic composition due to their high loss on ignition and componentry characteristics. Gray fields represent the compositional fields for Cotopaxi products considering Garrison et al. (2011) and Pistolesi et al. (2011) compositions for whole rock as well as glass.

composition (SiO_2 wt % = 56.94 ± 0.25) and low LOI (Table 1). These compositions fall in the fields defined by Garrison et al. (2011) and Pistolesi et al. (2011) for Cotopaxi andesitic products throughout the volcano history (Figure 7). The componentry analysis performed by Gaunt et al. (2016) indicates that for 24 August, hydrothermal material was already below 20%. Juvenile material displays two kinds of morphologies: blocky and porous grains (Gaunt et al., 2016). In both cases fresh glass is present in variable amounts.

SiO_2 contents of the analyzed matrix glass from our sampled juvenile fragments is between 65.5 and 76.2 wt % (data normalized to an anhydrous basis), falling in the compositional field of glass defined by Pistolesi et al. (2011), which ranges from 57 to 76 SiO_2 wt %. Here we observe two populations on our juvenile matrix glass, the low-silica group, dacitic in composition, is similar to the matrix glasses analyzed by Gaunt et al. (2016), whereas the other group is silica rich, displaying rhyolitic compositions. The samples showing high-silica glass display also a higher microlite crystallinity. Harker diagrams are shown in Figure 7. K_2O shows a positive correlation with SiO_2 , while MgO , Al_2O_3 , CaO , TiO_2 , and FeO display negative trends. This could be interpreted as a typical differentiation process due to the late crystallization of plagioclase and pyroxene (opx and cpx; Figure 7), consistent with observed phenocryst and microlite phases in the ash samples, in addition to Fe oxides as magnetite. Sulfur was below detection limit in the matrix glasses, while chlorine and fluorine yielded 641 ± 27 and 250 ± 175 ppm ($n = 6$), respectively.

The juvenile glass was tested for equilibrium with plagioclase microlites, following the methods of Putirka (2008) and Waters and Lange (2015). Results are summarized in Table 1. Within our glass matrix and plagioclase microlite analyses, 42 combined pairs were useful for T, 15 for P, and 23 for H_2O estimations. For both models we used initial temperatures and pressures of 950 and 1,000°C and 200 and 400 MPa, following the findings of Martel et al. (2018) for magmatic conditions in Cotopaxi storage zones. Slightly higher temperatures are obtained when 400-MPa pressure is used. Changing initial temperature does not have any impact. Using equation 26 of Putirka (2008), we obtained equilibrium temperatures varying in response to the different initial pressures. Temperatures of $1,055 \pm 6^\circ\text{C}$ and $1,066 \pm 6^\circ\text{C}$ ($n = 14$) were obtained for low-silica glass. For high-silica glass the temperatures were 971 ± 6 and $981 \pm 6^\circ\text{C}$ ($n = 28$). These temperatures are in agreement with the andesitic nature of the bulk ash compositions, representing the composition of the bulk

magma. Water contents obtained by equation 25b (Putirka, 2008) are around 1 wt % for both glass compositions and initial pressures. The Waters and Lange (2015) geohygrometer yields slightly different results, 1.1 ± 0.5 -wt % H₂O and 0.8 ± 0.2 -wt % H₂O using 1,000°C and 400 MPa as initial conditions for low- and high-silica glasses, respectively, and 2.0 ± 0.5 -wt % H₂O and 1.7 ± 0.17 -wt % H₂O using 950°C and 200 MPa as initial conditions. These water contents are similar to those measured in melt inclusions from neighboring Tungurahua volcano, from 0.4 to 2.4, but clustering between 0.8 and 1.6 H₂O wt % (Myers et al., 2014). The last equilibrium pressure among matrix glass and plagioclase microlite is more difficult to estimate as the error can be high. Using 200 and 400 MPa as initial pressure, we obtain 220 ± 97 and 244 ± 98 for low-silica glass. These pressure ranges encompass depths from 4.9 to 13.2 km assuming a crustal density of 2,600 kg/m³. High-silica glass did not yield suitable pressures using Putirka (2008) equations. We then tested the Ab¹ in haplograntic glass geobarometer (Hammer & Rutherford, 2003) for rhyolitic matrix glasses, more appropriate for our high-silica glass compositions. Only five of our glass analyses fulfill the geobarometer requirements (i.e., normative Ab + Or + Qz > 90, An < 20 and Cor < 2) and lead to P_{H₂O} pressures from 56 to 193 MPa. These pressures are equivalent to 2.2 to 7.4 km below the crater and are consistent with the models of Molina et al. (2008) and Hickey et al. (2015) for the unrest of Cotopaxi observed by seismicity and deformation in 2001. According to Molina et al. (2008), the seismicity recorded in 2001 was associated with the resonance of a crack located 2–3 km beneath the northeastern flank, which was opened due to particle-laden gases released from a deeper magmatic intrusion. To explain the deformation observed in 2001 and measured by electronic distance measurement (EDM), Hickey et al. (2015) proposed a small oblate-shaped source 4–5 km beneath the summit. Their source is, however, located southwest of the summit, and seismic activity is attributed to fluid migration from this source to the NW of the edifice. Pressures below 87 MPa (3.4 km) are able to explain the observed degassing as SO₂, HCl, and HBr exsolution from magma requires low pressures (Baker & Alletti, 2012). Morales Rivera et al. (2017) proposed a source model based on deformation data that would be located between 5.5 and 12.1 km below the summit. This reservoir is in agreement with the pressures obtained for low-silica glass. Two reservoir zones were imaged, indicating that magma could ascend from a reservoir zone as deep as 12–13 km (Morales Rivera et al., 2017) toward a shallower area at about 2- to 5-km depth in order to start degassing.

4. Discussion

In the following section we synthesize temporal observations of degassing and seismicity to characterize the processes leading to and culminating in the 2015 eruption of Cotopaxi. Figure 8 summarizes the measured parameters. Constraints on the potential volume of magma involved in this eruption are also discussed.

4.1. Chronological Evolution and Processes of the Preruptive and Eruptive Phases

4.1.1. Phase 1: Deep Magma Recharge and Initial Interaction With the Hydrothermal System—1 April to 19 May

According to our analysis of the seismicity, the events detected at BREF seismic station before 1 April 2015, correspond mostly to IQs that were present at least since 2013. They are not directly related to the magmatic/volcanic activity. In contrast, the appearance of LPs at the beginning of April marks the start of the unrest (Figure 8a). We interpret this seismicity as the response of the hydrothermal system to the slow transfer of a magma batch from a deeper to a shallower reservoir. The high crystallinity of the analyzed ash grains (Gaunt et al., 2016) supports this slow ascent rate. The deep reservoir could be as deep as 13–12 km beneath the surface according to our low-silica glass-plagioclase equilibrium and to the model of Morales Rivera et al. (2017). This movement lasted for at least 6 weeks, and the progressive increase in LP seismicity might be related to the progressive heating and pressurization of the hydrothermal system. The permanent DOAS network did not detect any increase in the SO₂ emission from the background level at this time (Figure 8c). This can be explained by different hypotheses: Magma was deep enough to prevent SO₂ exsolution and outgassing, the hydrothermal system was scrubbing the magmatic SO₂, or the system was closed to degassing. Given the equilibrium pressures recorded by the high-silica glass, magma could have stalled for a short time around 7 km deep, where SO₂ degassing is still minimal.

4.1.2. Phase 2: Partial Unsealing of the Hydrothermal System and Appearance of SO₂—19 to 29 May

Phase 2 is characterized by a progressive decrease in LP activity, accompanied by the appearance of SO₂ degassing with low fluxes (309 ± 290 t/d) but with continuous detections (Figures 8a–8c). The increase of

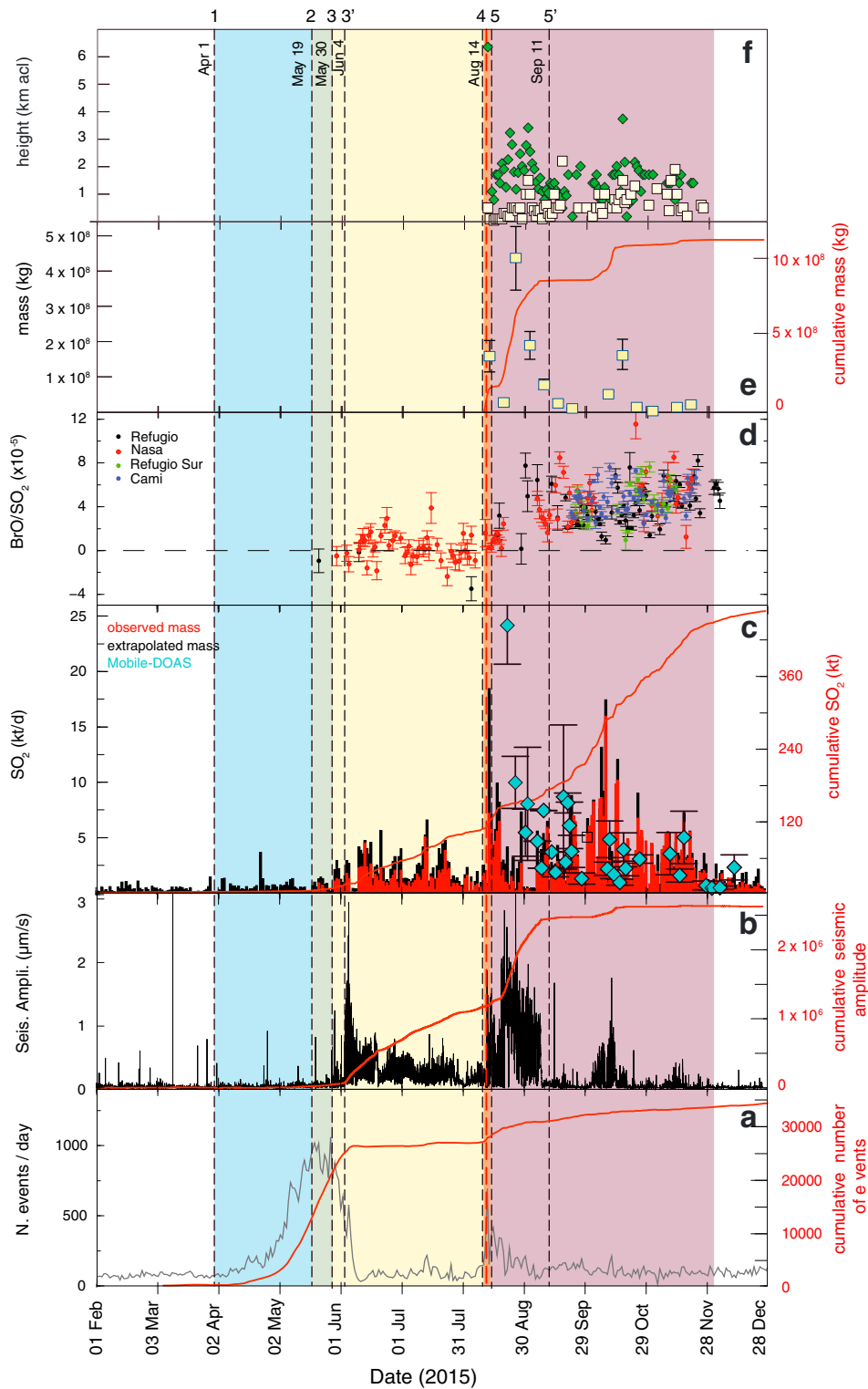


Figure 8. Composite figure of the measured parameters at Cotopaxi from 1 February to 31 December 2015. Numbers 1 to 5 indicate the beginning of discussed phases and key dates as in previous figures. Phases 1 to 5 are in blue, green, yellow, orange, and pink, respectively. (a) Number of transient events per day. (b) Median seismic amplitude. To detrend the integrals of the median amplitude and daily number of detections, integrations have been done after subtracting from the integrated data the average background values calculated prior to 1 April 2015. (c) SO₂ fluxes from permanent network and mobile-DOAS traverses and cumulative SO₂ since 1 April. (d) BrO/SO₂ ratios. (e) Emitted mass of ash measured directly from the field and curve of synthetic mass as detailed in Bernard et al. (2016). (f) Heights of eruptive columns in yellow as observed from Instituto Geofísico of the Escuela Politécnica Nacional video cameras and in green satellite data from the Volcanic Ash Advisory Center (Bernard et al., 2016).

water pressure in the hydrothermal system during the previous phase led to a partial unsealing of the system itself resulting in a drop in pressure, reflected by the lowered number of LPs. This partial unsealing and increased permeability would have also allowed the escape of SO₂. The presence of SO₂ implies that the intruding magma was at this time emplaced at a shallower depth corresponding to the pressure of 87 MPa (3.4 km) calculated for high-silica glass and allowing SO₂ exsolution (Baker & Alletti, 2012). To limit SO₂ scrubbing requires an isolation of the magmatic gases from the hydrothermal system or the disappearance of this system. The later hypothesis is in contradiction with the following phase (Phase III) when boiling of the hydrothermal system was observed. The limited scrubbing can be then explained by the model of the insulating vapor film developed at the boundaries of the hydrothermal system due to its progressive heating (Wohletz, 1986). This film would constitute a thermal barrier inhibiting direct contact of the fluids in the hydrothermal system with the magma. With this insulating barrier, the SO₂ released from the magma may have been able to escape to the atmosphere avoiding the scrubbing process (Symonds et al., 2001).

4.1.3. Phase 3: Boiling of the Hydrothermal System—30 May to 13 August

The number of LP events strongly dropped and transient events were replaced by a more continuous tremor on 4 June (Figures 8b and 8c). SO₂ detection was continuous and the fluxes reached $1,310 \pm 973$ t/d. At this point we argue that the heat of the intrusion started a film boiling process of the hydrothermal system (Wohletz, 1986; Wohletz et al., 2013), which produced seismic tremor. A low magma/water ratio is required to maintain this process working without a superheating that would cause sudden expansion and explosion of the system. The opal minerals observed in the first solid material emitted by Cotopaxi (Gaunt et al., 2016) might preserve evidence for discrete, nonexplosive magma-water interactions. An increase in SO₂ flux could also be attributed to shallowing of magma. Such high SO₂ emissions also require that scrubbing was not an active process, further supporting the idea of very restricted or nonexistent contact between the magma and the hydrothermal system. The presence of BrO in the gas plume as observed starting on 4 June (Figure 8d) and the presence of HCl, measured on 6 August, are also consistent with a shallow magma body. HBr (the precursor of BrO; Oppenheimer et al., 2006), and HCl both require a lower pressure and dry pathway to escape given their high distribution coefficient into hydrous fluids (Bureau et al., 2000).

Interestingly, on 22 July a green lake was observed in Cotopaxi crater. Sampling this lake was impossible at the time given the safety concerns of accessing the crater. The small decrease in SO₂ emission observed during the first week of August could be associated with a weak scrubbing process produced by the presence of this lake. This lake might have resulted from the partial melting of the inner crater glacier as hot gases were continuously passing by and not necessarily by ascent of hydrothermal fluids.

4.1.4. Phase 4: Superheating and Expansion of the Hydrothermal System—13 and 14 August

The explosive behavior observed on 14 August can be explained by either of two processes described by Wohletz (1986): (1) spontaneous nucleation (superheating) or (2) thermal detonation. Both processes require a period of “film boiling” before the explosive behavior, which is represented by the June–August tremor activity. The cracking produced by the superheating and resulting overpressure could have produced the families of VT events observed prior to the explosions (Figure 8a). Subsequently, the thermal detonation or expansion should have been triggered by the pressure waves produced by the failure of the conduit material. This led to fine fragmentation and rapid collapse of the insulation film resulting in rapid heat transfer and vapor production, finally leading to the four hydromagmatic explosions of 14 August (Bernard et al., 2016; Gaunt et al., 2016). The volume of juvenile magma involved in those explosions was small (~26%, Gaunt et al., 2016). Despite the high-altitude columns reaching up to 9 km above the crater, the total emitted mass of solid material from these explosions was small: $1.58 \pm 0.45 \times 10^8$ kg, equivalent to a bulk deposit volume of $1.18 \pm 0.33 \times 10^5$ m³ (Bernard et al., 2016; Figures 8e–8f). This leads us to the conclusion that the observed columns consisted mainly of gases issued from rapid decompression of the magma and from partial volatilization of what was still left of the hydrothermal system after the boiling period. Hence, the decompression wave leading to the explosions should also have allowed a rapid gas exsolution explaining the high SO₂ emission observed by satellites on 14 August and should have increased the magma ascent rate leading to the impending ash venting activity and increase in BrO/SO₂ ratios.

4.1.5. Phase 5: Ash Venting: 15 August–Late November

Geophysical parameters, as well as the nature of the emitted products point out to rapid evolution from the hydromagmatic activity to a magmatic process. Magmatic activity dominated the eruption from 15 August until its waning in late November.

The hydromagmatic explosions were followed by several phases of ash venting characterized by sustained tremor directly correlated with the mass emission rate (Bernard et al., 2016) and roughly with the SO₂ emission rate (Figures 8e and 8f). During this phase, BrO and HCl were also detected together with low CO₂/SO₂ ratios, typical of a shallow magmatic source and open vent degassing (Aiuppa et al., 2017). Bulk ash composition was homogenous and andesitic in nature, typical of Cotopaxi magmatic activity (Hall & Mothes, 2008; Pistolesi et al., 2011). The ash columns reached a maximum of 6-km height above the crater level but were typically less than 3.5 km above the crater level. The erupted grain size was very fine indicating a very effective fragmentation process. Bernard et al. (2016) divided this phase in three episodes according to tremor amplitude and the amount of erupted ash. Each episode showed a decrease in the maximum recorded tremor amplitude, duration, and mass of emitted ash.

All the monitored parameters returned to near background levels by the end of November including the reappearance of families of IQs. The number of these events was higher when the tremor amplitude was lower (Figure 8b). They slowly reappeared after 11 September, but once the tremor completely vanished on 30 November, the IQs became permanently present in the same number as before the beginning of the unrest (Figure 2b). No or very few VT events were recorded after 11 September, indicating that the overpressure in the system was negligible and that the ash emissions were produced by only a small volume of remnant magma that progressively lost volatiles. These remaining VTs could be due to gravitational readjustment of the volcanic edifice after the main eruptive activity. Once the magma became gas depleted, the eruption progressively waned. At the time of writing only a small, SO₂-poor (less than 50 t/d) gas emission is still observed at the volcano crater (Figure 8c). This emission rate is close to the preeruption SO₂ background emission rate (27 ± 26 t/d).

4.2. Volume of Degassing Magma

Juvenile material displays two kinds of morphologies: blocky and porous grains (Gaunt et al., 2016). In both cases fresh glass is present in variable amounts. Phenocrysts and microlites of plagioclase and orthopyroxene are present in the juvenile ash fragments, but no melt inclusions are observed, precluding the analysis of the preeruptive volatile concentration in the juvenile magma. Despite this fact, we estimated the minimum volume of magma necessary to produce the measured SO₂ outgassing, considering the typical volatile contents in andesitic magmas and a complete SO₂ degassing. Given the high SO₂ emission rates measured at Cotopaxi, and the absence of S in the analyzed juvenile glasses, we believe that assuming complete SO₂ degassing is plausible. This is also supported by the texture of juvenile microlite particles showing evidence of gas-driven filter pressing (Gaunt et al., 2016).

A total of 470 kt of SO₂ was emitted by Cotopaxi during the 2015 eruptive period, based on the continuous DOAS measurements. The uncertainty in this value is at least 30%, considering large variations in the variables involved in the gas flux calculations (e.g., Galle et al., 2010). Assuming that most of measured SO₂ was magmatic, we used the approach of Self et al. (2004) to estimate the volume of degassing magma required to produce the measured SO₂ emission. Two different S-initial contents were used in order to encompass the S measured in melt inclusions in andesitic magmas: (1) Tungurahua 2006 andesites, similar in composition to Cotopaxi products, displaying melt inclusions with S contents up to 1,800 ppm (Myers et al., 2014) and (2) Lascar 1989 andesites showing a very high S content of 4,400 ppm in melt inclusions (Shinohara, 2008). We used a crystallinity of 20% as observed in our samples. Total emitted SO₂ would require $1.63 \times 10^{11} \pm 6.93 \times 10^{10}$ kg of magma, which corresponds to a volume of $65.3 \times 10^6 \pm 27.7 \times 10^6$ m³, considering the 30% uncertainty in the SO₂ estimation, for the first case. For the second case, we obtained a mass of magma of $6.68 \times 10^{10} \pm 2.84 \times 10^{10}$ kg with a corresponding volume of $26.7 \times 10^6 \pm 11.3 \times 10^6$ m³.

Morales Rivera et al. (2017) proposed that the deformation estimated using COSMO-SkyMed interferometric synthetic aperture radar and continuous GPS prior to the eruption is consistent with an opening volume of 6.8×10^6 m³. The modeled inclined sheet intrusion is located 7 km SSE of the crater. According to their analysis, this volume did not erupt but could have put shallower storage zones in a critical state, promoting failure and eruption. In any case, this calculated volume change is much lower than the expected volume estimated on the basis of the SO₂ emitted mass, even considering a very S-rich magma (e.g., 1989 Lascar andesites). On the other hand, Mothes et al. (2016), using CGPS data including a station located 20 km from the volcano, find a source located 24.2 km below the crater with a volume increase of $41.8 \pm 26 \times 10^6$ m³ for

the same preeruptive time frame. This volume is in better agreement with our volume estimates. However, we note that the inferred source depth is too high for the volatiles in the magma to exsolve.

Taking into account the total mass of emitted ash during the whole period (1.2×10^9 kg~ 8.59×10^5 -m³ bulk deposit, Bernard et al., 2016) and the juvenile content (70–85%, Gaunt et al., 2016), our results show that less than 2% of the mass of degassing magma was actually emitted during this eruption. Considering the smaller intruded volume estimated by InSAR, only 6% of solid juvenile material would have been emitted. This is supported by the volumetric considerations presented by Arnold et al. (2018) indicating that a volume of $5\text{--}15 \times 10^5$ m³ was removed from the edifice during this eruption. This value is already as high as the total volume estimated for the bulk deposit. Excess degassing is inferred based on these data. Several mechanisms are proposed in the literature to explain this feature rather common at arc volcanoes: gas escape from convective magma overturn in the conduit (Stevenson & Blake, 1998), gas flow through a permeable stagnant magma-filled conduit (Edmonds et al., 2003), the free gas-phase model (Wallace & Gerlach, 1994), and breakdown of sulfur-bearing magmatic phases (Witter et al., 2005), among others. Defining which mechanism is responsible for the excess sulfur for this eruptive phase at Cotopaxi is beyond the scope of this work. Nevertheless, a magma convection mechanism (Stevenson & Blake, 1998), between the deeper (12-km, InSAR deformation source) and shallower (7–2 km) pressures (calculated from high-silica matrix glasses) might explain the large amount of measured SO₂ compared to the amount of solid magma emitted.

5. Conclusions

We examined degassing, seismic, and geochemical data recorded during the 2015 unrest and eruption of Cotopaxi volcano in order to better understand the temporal evolution and origin of this eruption.

Our time series analyses show that seismic activity and SO₂ outgassing were clear precursors of the 14 August 2015 eruption. First, during April–May 2015, the transient seismicity was dominated by LP events, possibly induced by heating of the hydrothermal system due to a magmatic intrusion. SO₂ was first detected mid-May when LP activity was at the highest level, suggesting that gas-rich magma was ascending to shallow depths in the conduit at that time. At the beginning of June, the seismicity evolved from transient LP events to tremor, accompanying an increase in SO₂ degassing and the appearance of BrO in the plume, indicating an even shallower magmatic source. SO₂ emission and tremor persisted at variable levels until 13 August when swarms of small VTs preceded and accompanied the 14 August hydromagmatic explosions. We interpret this explosive phase as being caused by the effective interaction of magma with the hydrothermal system. This process resulted in the rapid heat transfer and vapor production, leading to the hydromagmatic explosions. These were followed by several episodes of ash emissions mostly accompanied by emission tremor and a progressive decay of the activity until November 2015. This is interpreted as the progressive depletion of the eruptible material and coeval decompression of the system.

Total unrest and eruption lasted for 8 months with ash emission taking place over 14 weeks following the 14 August explosions. A magmatic signature of the emitted gas, beginning with the hydromagmatic explosions, is evidenced by the high SO₂ fluxes (up to 24 kt/d), the presence of BrO (BrO/SO₂ ratios > $5\text{--}10 \times 10^{-5}$) and HCl (SO₂/HCl > 5.8), the absence of H₂S in the plume and the low CO₂/SO₂ ratios (0.6 to 2.1). At least 470 kt of SO₂ was released in the atmosphere during the whole unrest and eruptive phase. Bulk ash and matrix glass chemistry of the juvenile grains indicate an andesitic bulk juvenile magma having suffered a differentiation process leading to the presence of dacitic to rhyolitic glass. The absence of S measured in the matrix glass indicates complete exsolution and degassing of S from the melt. This intense degassing could have rapidly depleted magma in volatiles precluding any further explosive activity. Magma volume estimated on the basis of the 470 kt of SO₂ assuming a preeruptive S content of 1,800 or 4,400 ppm in the magma exceeds more than 50 times the total volume of erupted solid juvenile material. This excess sulfur degassing may indicate that a considerable volume of unerupted but highly degassed magma remains below the edifice. If a stiff plug has been formed, a highly explosive scenario should be considered in the hazard assessment for the next reactivation of the volcano. Historical reports of Cotopaxi activity show that both short-duration (months) and long-duration (years) eruptive periods usually start with mild eruptive phases and culminate in VEI 3–4 paroxysms. Therefore, special care should be taken in continuing monitoring Cotopaxi, aiming to identify precursory signs of an eventual larger eruption such as a new magma recharge being able to rejuvenate the system.

Acknowledgments

We would like to acknowledge the technical staff of Instituto Geofísico for their hard work during the crisis that allowed obtaining continuous data sets. Broadband stations used in this study are part of the JICA collaboration with the IG-EPN. The Ministerio Coordinador de la Seguridad and the Fuerza Aérea Ecuatoriana (FAE) provided flights for plume measurements. Patricio Ramón is kindly acknowledged for coordinating monitoring flights. The Secretaría de Gestión del Riesgo facilitated fieldwork for NOVAC installations. U.S. Geological Survey/VDAP is kindly acknowledged for providing the Multi-GAS instrument. David Griffith is thanked for letting us use his MALT/FTIR code. Meteorological simulations were performed at the High Performance Computing system at the USFQ. This research has been conducted in the context of the Laboratoire Mixte International "Séismes et Volcans dans les Andes du Nord" of IRD. BrO/SO₂ ratios were part of the DFG Project PL 193/14-1, including University of Heidelberg and IG-EPN. We kindly acknowledge Jean-Luc Devidal for his invaluable help in preparing and analyzing ash grains at the electron microprobe. We are also grateful to Alicia Guevara for the bulk ash analyses performed at the Departamento de Metalurgia Extractiva (EPN). Taryn Lopez, Heather Wright, and an anonymous reviewer are kindly acknowledged for their thoughtful comments that improved the manuscript. We also thank Marie Edmonds for the editorial handling. Any use of trade, firm, or product names is for descriptive purposes only and does not imply endorsement by the U.S. Government. The gas data used in this manuscript is available on EarthChem Library <http://dx.doi.org/10.1594/IEDA/111165>.

References

- Aiuppa, A. (2009). Degassing of halogens from basaltic volcanism: Insights from volcanic gas observations. *Chemical Geology*, 263(1-4), 99–109. <https://doi.org/10.1016/j.chemgeo.2008.08.022>.
- Aiuppa, A., Fischer, T. P., Plank, T., Robidoux, P., & Di Napoli, R. (2017). Along-arc, inter-arc and arc-to-arc variations in volcanic gas CO₂/S₂ ratios reveal dual source of carbon in arc volcanism. *Earth Science Reviews*, 168, 24–47. <https://doi.org/10.1016/j.earscirev.2017.03.005>
- Aiuppa, A., Moretti, R., Federico, C., Giudice, G., Gurrieri, S., Liuzzo, M., et al. (2007). Forecasting Etna eruptions by real-time observation of volcanic gas composition. *Geology*, 35(12), 1115–1118. <https://doi.org/10.1130/G24149A.1>
- Arnold, D. W. D., Biggs, J., Wadge, G., & Mothes, P. (2018). Using satellite radar amplitude imaging for monitoring syn-eruptive changes in surface morphology at an ice-capped stratovolcano. *Remote Sensing of Environment*, 209, 480–488. <https://doi.org/10.1016/j.rse.2018.02.040>
- Baker, D. R., & Alletti, M. (2012). Fluid saturation and volatile partitioning between melts and hydrous fluids in crustal magmatic systems: The contribution of experimental measurements and solubility models. *Earth-Sciences Reviews*, 114, 298–324. <https://doi.org/10.1016/j.earscirev.2012.06.005>
- Battaglia, J., Métaixian, J.-P., & Garaebiti, E. (2016). Families of similar events and modes of oscillation of the conduit at Yasur volcano (Vanuatu). *Journal of Volcanology and Geothermal Research*, 322, 196–211. <https://doi.org/10.1016/j.jvolgeores.2015.11.003>
- Bernard, B. (2013). Homemade ashmeter: A low-cost, high-efficiency solution to improve tephra field-data collection for contemporary explosive eruptions. *Journal of Applied Volcanology*, 2(1), 1. <https://doi.org/10.1186/2191-5040-2>
- Bernard, B., Battaglia, J., Proaño, A., Hidalgo, S., Vásconez, F., Hernandez, S., & Ruiz, M. (2016). Relationship between volcanic ash fallouts and seismic tremor: Quantitative assessment of the 2015 eruptive period at Cotopaxi volcano, Ecuador. *Bulletin of Volcanology*, 78(11), 80. <https://doi.org/10.1007/s00445-016-1077-5>
- Bourquin, J., Hidalgo, S., Arellano, S., Troncoso, L., Galle, B., Arrais, S., & Vásconez, F. (2009). First observations of intermittent, non-eruptive gas emissions of Cotopaxi volcano (Ecuador) during a period of heightened seismicity. *Eos Trans. AGU*, 90 (52), Fall Meet. Suppl., Abstract V23D-2140.
- Bureau, H., Keppler, H., & Métrich, N. (2000). Volcanic degassing of bromine and iodine: Experimental fluid/melt partitioning data and applications to stratospheric chemistry. *Earth and Planetary Science Letters*, 183(1-2), 51–60. [https://doi.org/10.1016/S0012-821X\(00\)00258-2](https://doi.org/10.1016/S0012-821X(00)00258-2)
- Chouet, B. A. (1996). Long-period volcano seismicity: Its source and use in eruption forecasting. *Nature*, 380(6572), 309–316. <https://doi.org/10.1038/380309a0>
- Dinger, F., Bobrowski, N., Warnach, S., Bredmeyer, S., Hidalgo, S., Arellano, S., et al. (2018). Periodicity in the BrO/SO₂ molar ratios in the volcanic gas plume of Cotopaxi and its correlation with the Earth tides during the eruption in 2015. *Solid Earth Discussions*. <https://doi.org/10.5194/se-2017-89>
- Edmonds, M., Oppenheimer, C., Pyle, D. M., Herd, R. A., & Thompson, G. (2003). SO₂ emissions from Soufrière Hills Volcano and their relationship to conduit permeability, hydrothermal interaction and degassing regime. *Journal of Volcanology and Geothermal Research*, 124(1-2), 23–43. [https://doi.org/10.1016/S0377-0273\(03\)00041-6](https://doi.org/10.1016/S0377-0273(03)00041-6).
- Galle, B., Johansson, M., Rivera, C., Zhang, Y., Kihlman, M., Kern, C., et al. (2010). Network for Observation of Volcanic and Atmospheric Change (NOVAC)—A global network for volcanic gas monitoring: Network layout and instrument description. *Journal of Geophysical Research*, 115, D05304. <https://doi.org/10.1029/2009JD011823>
- Garrison, J. M., Davidson, J. P., Hall, M., & Mothes, P. (2011). Geochemistry and petrology of the most recent deposits from Cotopaxi Volcano, Northern Volcanic Zone, Ecuador. *Journal of Petrology*, 52(9), 1641–1678. <https://doi.org/10.1093/ptrology/egr023>
- Gaunt, H. E., Bernard, B., Hidalgo, S., Proaño, A., Wright, H., Mothes, P., et al. (2016). Juvenile magma recognition and eruptive dynamics inferred from the analysis of ash time series: The 2015 reawakening of Cotopaxi volcano. *Journal of Volcanology and Geothermal Research*, 328, 134–146. <https://doi.org/10.1016/j.jvolgeores.2016.10.013>
- Green, D., & Neuberg, J. (2006). Waveform classification of volcanic low-frequency earthquake swarms and its implication at Soufrière Hills Volcano, Montserrat.
- Griffith, D. W. T. (1996). Synthetic calibration and quantitative analysis of gas-phase FT-IR spectra. *Applied Spectroscopy*, 50, 59–70. <https://doi.org/10.1366/0003702963906627>
- Gunawan, H., Caudron, C., Pallister, J., Primulyana, S., Christenson, B., McCausland, W., et al. (2017). New insights into Kawah Ijen's volcanic system from the wet volcano workshop experiment. In T. Ohba, B. Capaccioni, & C. Caudron (Eds.), *Geochemistry and Geophysics of Active Volcanic Lakes* (Vol. 437, pp. 35–56). London: Geological Society of London. <https://doi.org/10.1144/SP437.7>
- Hall, M., & Mothes, P. (2008). The rhyolitic-andesitic eruptive history of Cotopaxi volcano, Ecuador. *Bulletin of Volcanology*, 70(6), 675–702. <https://doi.org/10.1007/s00445-007-0161-2>
- Hammer, J. E., & Rutherford, M. J. (2003). Petrologic indicators of preeruption magma dynamics. *Geology*, 31(1), 79–82. [https://doi.org/10.1130/0091-7613\(2003\)031<0079:PIOPMD>2.0.CO;2](https://doi.org/10.1130/0091-7613(2003)031<0079:PIOPMD>2.0.CO;2)
- Helmstetter, A., Nicolas, B., Comon, P., & Gay, M. (2015). Basal icequakes recorded beneath an Alpine glacier (Glacier d'Argentière, Mont Blanc, France): Evidence for stick-slip motion? *Journal of Geophysical Research: Earth Surface*, 120, 379–401. <https://doi.org/10.1002/2014JF003288>
- Hickey, J., Gottsmann, J., & Mothes, P. (2015). Estimating volcanic deformation source parameters with a finite element inversion: The 2001–2002 unrest at Cotopaxi volcano, Ecuador. *Journal of Geophysical Research: Solid Earth*, 120, 1473–1486. <https://doi.org/10.1002/2014JB011731>
- Hidalgo, S., Battaglia, J., Arellano, S., Steele, A., Bernard, B., Bourquin, J., et al. (2015). SO₂ degassing at Tungurahua volcano (Ecuador) between 2007 and 2013: Transition from continuous to episodic activity. *Journal of Volcanology and Geothermal Research*, 298, 1–14. <https://doi.org/10.1016/j.jvolgeores.2015.03.022>
- Johansson, M. (2009). Application of Passive DOAS for Studies of Megacity Air Pollution and Volcanic Gas Emissions, (PhD thesis, 64 pp.). Chalmers University of Technology.
- Johansson, M., Galle, B., Zhang, Y., Rivera, C., Chen, D., & Wyser, K. (2009). The dual-beam mini-DOAS technique—measurements of volcanic gas emission, plume height and plume speed with a single instrument. *Bulletin of Volcanology*, 71, 747–751. <https://doi.org/10.1007/s00445-008-0260-8>
- Kelly, P. J., Kern, C., Roberts, T. J., Lopez, T., Werner, C., & Aiuppa, A. (2013). Rapid chemical evolution of tropospheric volcanic emissions from Redoubt Volcano, Alaska, based on observations of ozone and halogen-containing gases. *Journal of Volcanology Geothermal Research*, 259, 317–333. <https://doi.org/10.1016/j.jvolgeores.2012.04.023>
- Kern, C., Deutschmann, T., Vogel, L., Wehrbach, M., Wagner, T., & Platt, U. (2010). Radiative transfer corrections for accurate spectroscopic measurements of volcanic gas emissions. *Bulletin of Volcanology*, 72(2), 233–247. <https://doi.org/10.1007/s00445-009-0313-7>

- Lübcke, P., Bobrowski, N., Arellano, S., Galle, B., Garzón, G., Vogel, L., & Platt, U. (2014). BrO/SO₂ molar ratios from scanning DOAS measurements in the NOVAC network. *Solid Earth*, 5(1), 409–424. <https://doi.org/10.5194/se-5-409-2014>
- Martel, C., Andújar, J., Mothes, P., Scaillet, B., Pichavant, M., & Molina, I. (2018). Storage conditions of the mafic and silicic magmas at Cotopaxi, Ecuador. *Journal of Volcanology and Geothermal Research*, 354, 74–86. <https://doi.org/10.1016/j.jvolgeores.2018.02.006>
- Métaxian, J.-P., Araujo, S., Mora, M., & Lesage, P. (2003). Seismicity related to the glacier of Cotopaxi Volcano, Ecuador. *Geophysical Research Letters*, 30(9), 1483. <https://doi.org/10.1029/2002GL016773>
- Michalakes, J., Dudhia, J., Gill, D., Henderson, T., Klemp, J., Skamarock, W., & Wang, W. (2005). The weather research and forecast model: Software architecture and performance. In *Proceedings of the eleventh ECMWF workshop on the use of high performance computing in meteorology* (pp. 156–168). Singapore: World Scientific.
- Millán, M. M. (1980). Remote sensing of air pollutants. A study of some atmospheric scattering effects. *Atmospheric Environment*, 1967(14), 1241–1253.
- Molina, I., Kumagai, H., García-Aristizábal, A., Nakano, M., & Mothes, P. (2008). Source process of very-long-period events accompanying long-period signals at Cotopaxi Volcano, Ecuador. *Journal of Volcanology and Geothermal Research*, 176(1), 119–133. <https://doi.org/10.1016/j.jvolgeores.2007.07.019>
- Morales Rivera, A. M., Amelung, F., Mothes, P., Hong, S.-H., Nocquet, J.-M., & Jarrin, P. (2017). Ground deformation before the 2015 eruptions of Cotopaxi volcano detected by InSAR: Cotopaxi ground deformation. *Geophysical Research Letters*, 44, 6607–6615. <https://doi.org/10.1002/2017GL073720>
- Mori, T., Mori, T., Kazahaya, K., Ohwada, M., Hirabayashi, J.-i., & Yoshikawa, S. (2006). Effect of UV scattering on SO₂ emission rate measurements. *Geophysical Research Letters*, 33, L17315. <https://doi.org/10.1029/2006GL026285>
- Mothes, P., Hall, M. L., Andrade, D., Yepes, H., Pierson, T. C., Gorki Ruiz, A., & Samaniego, P. (2004). Character, stratigraphy and magnitude of historical lahars of Cotopaxi volcano (Ecuador). *Acta Vulcanologica*, 16, 1000–1023.
- Mothes, P., Nocquet, J.-M., Morales, A., Jarrin, P., Gaunt, H.E., Yepes, M., & Viracucha, G. (2016). Geodetic signature of 2015–16 unrest at Cotopaxi-Ecuador: Modeling of GPS data, a deep magma source, synchronous seismic swarms and petrologic constraints. Cities on Volcanoes-9, At Puerto Varas, Chile, Volume: 53.4. ResearchGate. Presented at the Cities on Volcanoes, Puerto Varas, Chile.
- Mothes, P. A., Ruiz, M. C., Viracucha, E. G., Ramón, P. A., Hernández, S., Hidalgo, S., et al. (2017). Geophysical Footprints of Cotopaxi's Unrest and Minor Eruptions in 2015: An Opportunity to Test Scientific and Community Preparedness. In *Advances in Volcanology* (pp. 1–30). Berlin, Heidelberg: Springer. https://doi.org/10.1007/11157_2017_10
- Myers, M. L., Geist, D. J., Rowe, M. C., Harpp, K. S., Wallace, P. J., & Dufek, J. (2014). Replenishment of volatile-rich mafic magma into a degassed chamber drives mixing and eruption of Tungurahua volcano. *Bulletin of Volcanology*, 76. [https://doi.org/10.1007/s00445-014-0872-0\(11\)](https://doi.org/10.1007/s00445-014-0872-0(11))
- Neuberg, J., Luckett, R., Baptie, B., & Olsen, K. (2000). Models of tremor and low-frequency earthquake swarms on Montserrat. *Journal of Volcanology and Geothermal Research*, 101(1-2), 83–104. [https://doi.org/10.1016/S0377-0273\(00\)00169-4](https://doi.org/10.1016/S0377-0273(00)00169-4)
- Oppenheimer, C., Tsanev, V. I., Braban, C. F., Cox, R. A., Adams, J. W., Aiuppa, A., et al. (2006). BrO formation in volcanic plumes. *Geochimica et Cosmochimica Acta*, 70(12), 2935–2941. <https://doi.org/10.1016/j.gca.2006.04.001>
- Parra, R., Bernard, B., Narváez, D., Le Pennec, J.-L., Hasselle, N., & Folch, A. (2016). Eruption source parameters for forecasting ash dispersion and deposition from volcanic eruptions at Tungurahua volcano: Insights from field data from the July 2013 eruption. *Journal of Volcanology and Geothermal Research*, 309, 1–13. <https://doi.org/10.1016/j.jvolgeores.2015.11.001>
- Pistolesi, M., Rosi, M., Cioni, R., Cashman, K. V., Rossotti, A., & Aguilera, E. (2011). Physical volcanology of the post-twelfth-century activity at Cotopaxi volcano, Ecuador: Behavior of an andesitic central volcano. *Geological Society of America Bulletin*, 123(5-6), 1193–1215. <https://doi.org/10.1130/B30301.1>
- Podolsky, E. A., & Walter, F. (2016). Cryoseismology. *Reviews of Geophysics*, 54, 708–758. <https://doi.org/10.1002/2016RG000526>
- Putirka, K. D. (2008). Thermometers and barometers for volcanic systems. *Reviews in Mineralogy and Geochemistry*, 69(1), 61–120. <https://doi.org/10.2138/rmg.2008.69.3>
- Pyle, D. M. (2015). Sizes of volcanic eruptions. In *The encyclopedia of volcanoes* (pp. 257–264). London: Elsevier. <https://doi.org/10.1016/B978-0-12-385938-9.00013-4>
- Rodgers, M., Smith, P. J., Mather, T. A., & Pyle, D. M. (2016). Quiescent-explosive transitions during dome-forming volcanic eruptions: Using seismicity to probe the volcanic processes leading to the 29 July 2008 vulcanian explosion of Soufrière Hills Volcano, Montserrat. *Journal of Geophysical Research: Solid Earth*, 121, 8453–8471. <https://doi.org/10.1002/2016JB013180>
- Self, S., Gertisser, R., Thordarson, T., Rampino, M. R., & Wolff, J. A. (2004). Magma volume, volatile emissions, and stratospheric aerosols from the 1815 eruption of Tambora. *Geophysical Research Letters*, 31, L20608. <https://doi.org/10.1029/2004GL020925>
- Shinohara, H. (2008). Excess degassing from volcanoes and its role on eruptive and intrusive activity. *Reviews in Geophysics*, 46, 46. <https://doi.org/10.1029/2007RG000244>
- Shinohara, H., Aiuppa, A., Giudice, G., Gurrieri, S., & Liuzzo, M. (2008). Variation of H₂O/CO₂ and CO₂/SO₂ ratios of volcanic gases discharged by continuous degassing of Mount Etna volcano, Italy. *Journal of Geophysical Research*, 113, B09203. <https://doi.org/10.1029/2007JB005185>
- Skamarock, W. C., Klemp, J. B., Dudhia, J., Gill, D. O., Barker, D. M., Wang, W., & Powers, J. G. (2005). A description of the advanced research WRF version 2 (no. ncar/tn-468+str). National Center for Atmospheric Research Boulder CO Mesoscale and Microscale Meteorology Div.
- Stevenson, D. S., & Blake, S. (1998). Modelling the dynamics and thermodynamics of volcanic degassing. *Bulletin of Volcanology*, 60(4), 307–317. <https://doi.org/10.1007/s004450050234>
- Symonds, R. B., Gerlach, T. M., & Reed, M. H. (2001). Magmatic gas scrubbing: Implications for volcano monitoring. *Journal of Volcanology and Geothermal Research*, 108(1-4), 303–341. [https://doi.org/10.1016/S0377-0273\(00\)00292-4](https://doi.org/10.1016/S0377-0273(00)00292-4)
- Vallee, M., Nocquet, J.-M., Battaglia, J., Font, Y., Segovia, M., Regnier, M., et al. (2013). Intense interface seismicity triggered by a shallow slow slip event in the Central Ecuador subduction zone. *Journal of Geophysical Research: Solid Earth*, 118, 2965–2981. <https://doi.org/10.1002/jgrb.50216>
- Wallace, P. J., & Gerlach, T. M. (1994). Magmatic vapor source for sulfur dioxide released during volcanic eruptions: Evidence from Mount Pinatubo. *Science*, 265(5171), 497–499. <https://doi.org/10.1126/science.265.5171.497>
- Waters, L. E., & Lange, R. A. (2015). An updated calibration of the plagioclase-liquid hygrometer-thermometer applicable to basalts through rhyolites. *American Mineralogist*, 100(10), 2172–2184. <https://doi.org/10.2138/am-2015-5232>
- Weaver, C. S., & Malone, S. D. (1976). Mt. Saint Helens seismic events: Volcanic earthquakes or glacial noises? *Geophysical Research Letters*, 3, 197–200. <https://doi.org/10.1029/GL003i003p00197>
- Werner, C., Kelly, P. J., Doukas, M., Lopez, T., Pfeffer, M., McGimsey, R., & Neal, C. (2013). Degassing of CO₂, SO₂, and H₂S associated with the 2009 eruption of Redoubt Volcano, Alaska. *Journal of Volcanology and Geothermal Research*, 259, 270–284. <https://doi.org/10.1016/j.jvolgeores.2012.04.012>

- Witter, J. B., Kress, V. C., & Newhall, C. G. (2005). Volcán Popocatepetl, Mexico. Petrology, magma mixing, and immediate sources of volatiles for the 1994–present eruption. *Journal of Petrology*, *46*(11), 2337–2366. <https://doi.org/10.1093/petrology/egi058>
- Wohletz, K. H. (1986). Explosive magma-water interactions: Thermodynamics, explosion mechanisms, and field studies. *Bulletin of Volcanology*, *48*(5), 245–264. <https://doi.org/10.1007/BF01081754>
- Wohletz, K. H., Zimanowski, B., & Büttner, R. (2013). Magma-water interactions (Chapter 11) - Modeling Volcanic Processes. In S. Fagents, T. Gregg, & R. Lopes (Eds.), *Modeling Volcanic Processes* (pp. 230–256). Cambridge: Cambridge University Press.
- Zhang, Y., & Johansson, M. (2009). Mobile-DOAS software. Optical Remote Sensing Group Chalmers University of Technology, Sweden. Copyright © 2004–2009.